

We are IntechOpen, the world's leading publisher of Open Access books Built by scientists, for scientists

6,900

Open access books available

186,000

International authors and editors

200M

Downloads

Our authors are among the

154

Countries delivered to

TOP 1%

most cited scientists

12.2%

Contributors from top 500 universities



WEB OF SCIENCE™

Selection of our books indexed in the Book Citation Index
in Web of Science™ Core Collection (BKCI)

Interested in publishing with us?
Contact book.department@intechopen.com

Numbers displayed above are based on latest data collected.
For more information visit www.intechopen.com



Optically Controlled Laser-Plasma Electron Acceleration for Compact γ -Ray Sources

Serge Y. Kalmykov, Xavier Davoine,
Isaac Ghebregziabher and Bradley A. Shadwick

Additional information is available at the end of the chapter

<http://dx.doi.org/10.5772/intechopen.71679>

Abstract

Thomson scattering (TS) from electron beams produced in laser-plasma accelerators may generate femtosecond pulses of quasi-monochromatic, multi-MeV photons. Scaling laws suggest that reaching the necessary GeV electron energy, with a percent-scale energy spread and five-dimensional brightness over 10^{16} A/m², requires acceleration in centimeter-length, tenuous plasmas ($n_0 \sim 10^{17}$ cm⁻³), with petawatt-class lasers. Ultrahigh per-pulse power mandates single-shot operation, frustrating applications dependent on dosage. To generate high-quality near-GeV beams at a manageable average power (thus affording kHz repetition rate), we propose acceleration in a cavity of electron density, driven with an incoherent stack of sub-Joule laser pulses through a millimeter-length, dense plasma ($n_0 \sim 10^{19}$ cm⁻³). Blue-shifting one stack component by a considerable fraction of the carrier frequency compensates for the frequency red shift imparted by the wake. This avoids catastrophic self-compression of the optical driver and suppresses expansion of the accelerating cavity, avoiding accumulation of a massive low-energy background. In addition, the energy gain doubles compared to the predictions of scaling laws. Head-on collision of the resulting ultrabright beams with another optical pulse produces, via TS, gigawatt γ -ray pulses having a sub-20% bandwidth, over 10^6 photons in a microsteradian observation cone, and the observation cone, and the mean energy tunable up to 16 MeV.

Keywords: laser wakefield acceleration, optical control of injection, optical shock, negative chirp, pulse stacking, Thomson scattering, particle-in-cell simulations

1. Introduction

Particle accelerators are among the largest and most expensive scientific instruments. Their large footprint is dictated by the modest acceleration gradient (in tens of MeV per meter), limited by

the breakdown of metallic accelerating cavities. Accelerating electrons in the fully or partially ionized medium (i.e. a plasma) lifts this limitation, making accelerators thousands of times smaller, literally “table-top.” Since plasmas are free of the damage limits of conventional accelerators, they may build up TV/m fields within structures propagating at a near-luminal speed. First ideas of harnessing collective plasma fields to actively control the phase space of a high-energy electron beam (e-beam), were brought into the world over 60 years ago [1–3]. Yet, it was not until the first decade of this century that the accelerator community started witnessing systematic progress in plasma acceleration of electron and positron beams [4–8].

Competition with conventional linear accelerators in generation of quasi-monoenergetic (QME) e-beams requires independently driven near-luminal, high-field plasma structures, such as Langmuir plasma waves [9–11] or cavities (“bubbles”) of electron density [12–15]. The accelerating buckets must retain their shape in the course of propagation or change the shape and potentials in a controllable fashion to avoid degradation of the externally injected e-beam. It is equally important for the injection mechanism to ensure subsequent acceleration of the beam without picking up additional unwanted charge (the “dark current”). To this end, control over driver evolution and the plasma density profile is of paramount importance.

Driving the accelerating plasma structures with a radiation pressure of a femtosecond, multi-terawatt (TW) laser pulse (hence the term “laser wakefield”) provides abundant opportunities for all-optical control of both injection and acceleration processes [16, 17]. Early demonstrations of QME laser-plasma acceleration [4–6] were a perfect example of this control. It was not until the optical driver closely matched the plasma parameters, to ensure its propagation as a whole, without breaking up longitudinally or transversely, that the long coveted QME electron bunches were realized. The matching [18] made it possible for the laser to produce a “bubble” almost completely devoid of electrons in its immediate wake [19, 20]. The bubble acts at the same time as a nonlinear waveguide for the laser pulse and an accelerating bucket for the electrons. The ponderomotive force of the pulse maintains the bubble shape. It expels all electrons facing the pulse (hence the term “blowout regime”), while the bulk electrons are attracted to the propagation axis. The difference between attractive force due to the charge separation and the repulsive radial ponderomotive force controls the trajectories of electrons making up the bubble shell. The resulting soft channel, approximately replicating the three-dimensional (3-D) shape of the pulse [19], evolves in a lock-step with the optical driver [15, 16, 20–25]. In consequence, it traps initially quiescent background electrons, eliminating the need for an external photocathode [16, 21, 22]. Notably, in the regimes featuring production of low-emittance e-beams, only a tiny minority of electrons making up the bubble shell are trapped and subsequently accelerated. Their collective fields, i.e., beam loading [26], contribute very little to the bubble evolution and are unable to change the kinetics of self-injection [21–23].

Two fundamental relativistic optical phenomena underpin the matching conditions [18]. The first one is relativistic self-focusing. As electrons oscillate in the field of focused laser beam, the relativistic increase in their mass and, hence, the nonlinear refractive index reach maximum near axis, where the laser intensity is the highest. The plasma thus acts as a focusing fiber, compensating for diffraction. If the pulse power P exceeds the critical value $P_{\text{cr}} = 16.2(n_c/n_0)$ GW [27] even by a few percent, the self-focusing will saturate [28] only at the point of full

electron blowout [13]. Here, n_0 is the background electron density, $n_c = m_e \omega_0^2 / (4\pi e^2)$ is the critical density for radiation with a frequency ω_0 , and m_e and $-|e|$ are the electron rest mass and charge. Matching the spot size of the incident pulse to the value

$$r_m = 2^{3/2} k_p^{-1} (P/P_{cr})^{1/6} \quad (1)$$

balances the force due to the charge separation and the ponderomotive force acting upon the electron at the boundary of the bubble. Here, $k_p = \omega_{pe}/c = 1.88\sqrt{n_{20}} \mu\text{m}^{-1}$ is the plasma wave number, $\omega_{pe} = \sqrt{4\pi e^2 n_0 / m_e} \ll \omega_0$ is the Langmuir plasma frequency, c is the speed of light in vacuum, and n_{20} is the background density in units 10^{20} cm^{-3} . The matched pulse propagates in a single filament confined to the bubble. Conversely, strong mismatching results in a transverse breakup of the pulse, massive energy loss to the plasma, and disruption of self-guiding [29, 30]. The other key physical phenomenon, which limits electron energy gain, is self-phase-modulation, viz. accumulation of frequency red shift, imparted by the wake, at the self-phase-modulation. As the pulse propagates, this shift reaches a large fraction of ω_0 , while the negative group velocity dispersion (GVD) in the plasma delays these low-frequency components, etching away the pulse leading edge. In the frame of reference comoving with the bubble, these components start to accumulate around the point where electron density drops to zero¹, building up an optical shock with a subcycle rising edge [16, 22–25]. If the bubble were nonevolving, the etching velocity would be its phase velocity, which defines the electron dephasing length, $L_d = (2/3)(n_c/n_0)r_m$ [18]. In addition, etching velocity defines the pulse energy loss, which also limits electron energy gain. The pulse loses most of its energy and is unable to drive the bubble after a distance $L_{depl} = (n_c/n_0)c\tau_L$ (the depletion length), where τ_L is the duration of the incident pulse. Matching the dephasing and depletion lengths, so that $\tau_L = 2r_m/(3c)$, promises to maximize the acceleration efficiency and, possibly, reduce electron energy spread via phase space rotation at the end of acceleration cycle. Under the matching condition, the maximal energy gain scales as [18]

$$\Delta E[\text{GeV}] \sim 0.125(P[\text{PW}])^{1/3} \left(n_{20} \lambda_{0,\mu\text{m}}^2 \right)^{-2/3} \quad (2)$$

Here, $\lambda_{0,\mu\text{m}}$ is the laser pulse wavelength, $\lambda_0 = 2\pi c/\omega_0$, in microns. To ensure robust self-guiding and preserve self-injection, the power ratio must be at least $P/P_{cr} \equiv \kappa > 10$, or $n_{20} \lambda_{0,\mu\text{m}}^2 > 1.8 \times 10^{-4} \kappa (P[\text{PW}])^{-1} > 1.8 \times 10^{-3} (P[\text{PW}])^{-1}$. This, in combination with (2), yields a rather discouraging scaling,

$$\Delta E[\text{GeV}] < 40\kappa^{-2/3} P[\text{PW}] < 8.6P[\text{PW}] \quad (3)$$

According to (3), GeV energy gain in the matched regime requires at least 117 TW laser power, or 3.75 J per 32 fs matched pulse. The matched plasma density is, in this case, $n_0 = 2.4 \times 10^{18} \text{ cm}^{-3}$,

¹If electron evacuation is incomplete, and the frequency red shift is significant, the mid-IR radiation may further slide into the bubble, building inside it a single-cycle mid-IR pulse [31, 32] or even another optical shock [33, 34].

and the dephasing/depletion length is $L_d = 6.9$ mm. Laboratory experiments with cm-length gas jets from slit nozzles had approached this regime very closely, demonstrating background-free e-beams with the energy up to 900 MeV, yet at the repetition rate below 10 Hz [35]. Conversely, generating these near-GeV e-beams at a kHz repetition rate, for the applications dependent on dosage, would call for a 4 kW average-power laser amplifier, a technology of the distant future [36, 37]. Evidently, existing sub-50 TW systems are limited to the modest sub-450 MeV yields.

Apart from frustrating the production of GeV beams at a high repetition rate, this matching strategy only partly solves the problem of e-beam quality. While aiming to stabilize transverse dynamics and avoid filamentation of the drive pulse, the physical arguments leading to the scaling (2) assume that *the pulse self-compression remains unaltered*. Yet this process, apart from limiting the energy gain, destroys e-beam most assuredly if acceleration extends through the pulse depletion. (A plethora of evidence exists to this effect, both in laboratory experiments and numerical simulations [16, 19, 22–25, 38–42].) To enable a new generation of compact particle and radiation sources [43, 44], one has to bypass the limitations this of scaling by designing an optical driver resilient to self-phase-modulation and self-compression. Photon engineering of this kind, aiming to produce e-beams capable to emit quasi-monochromatic, high-flux γ -ray pulses via Thomson (or inverse Compton) scattering [44], is the focus of this chapter.

Inverse Compton scattering is an emerging radiation generation technique [25, 44–52], which has already shown its potential for obtaining quasi-monochromatic, strongly collimated γ -ray pulses through the collision of a short QME e-beam and a mid-IR to UV interaction laser pulse (ILP) [53–73]. During the interaction, relativistic electrons, propagating at an angle to the ILP, experience its Lorentz-compressed wave front, the maximum compression occurring along the e-beam direction. As they oscillate in the ILP electromagnetic field, electrons emit radiation, scattering the compressed wave front. An observer in the far field thus detects an angular distribution of high-energy photons, with the energy being the highest for a detector placed in the e-beam direction. For the head-on collision, the ILP photon energy is Doppler up-shifted by a factor $4\gamma_e^2$, where γ_e is the electron Lorentz factor. A beam of 900 MeV electrons thus converts 1.5 eV ILP photons into 19 MeV γ -photons. As the energy of emitted photons is much lower than the electron energy, the recoil is negligible. This low-energy semi-classical limit of the general quantum-mechanical inverse Compton scattering, known as Thomson scattering (TS), is the subject of this chapter. E-beams from conventional accelerators [53–62], produce multipicosecond TS γ -ray pulses. These have a high degree of polarization and are thus attractive as e-beam diagnostics [53, 54]. Their other applications are generation of polarized positrons from dense targets [55] and nuclear resonance fluorescence studies [56–61]. However, the large footprint of conventional accelerators makes such radiation sources scarce and busy user facilities. In addition, the large (cm-scale) size of the radio-frequency-powered acceleration cavities makes it difficult to generate and synchronize e-beams (and, hence, TS γ -ray pulses) on a subpicosecond time scale relevant to high-energy density physics [74]. Luckily, a miniature LPA offers an alternative technical solution that permits production of even shorter (viz. femtosecond), yet high-current (viz. kA) e-beams [75]. To drive narrowband TS γ -ray sources, these beams have to meet some minimal requirements, such as a combination of

a near-GeV energy with a percent-scale energy spread, a five-dimensional (5-D) brightness above 10^{16} A/m² [76], and preferably absent low-energy background. These requirements, in combination with the kHz-scale repetition rate dictated by the applications, are clearly conflicting even for the most ambitious laser technology [77, 78]. LPA experiments, guided by the theoretical scaling (2), are presently struggling to reach this level of performance. Typically, acceleration through pulse depletion, carried out in pursuit of ever higher energy, consistently builds up massive energy tails in the e-beams [39–42]. These beams produce a large-bandwidth γ -ray TS signal [63–73], which is incompatible with applications in nuclear photonics and radiography [48, 49, 60]. The current trend is to use the existing low-quality beams and try extending the high-energy tail of the photon distribution beyond 10 MeV, by using higher harmonics of the ILP [72], or by using few-GeV electrons from single-shot petawatt LPA facilities [73], or by employing an ILP of relativistic intensity [68].

Seeking the remedy to this situation, we take advantage of the fact that the LPA e-beams readily lend themselves to all-optical manipulation. Modifying the drive pulse dynamics, through a judicious choice of its phase and shape, alters kinetics of electron self-injection. This, in turn, introduces modulations to the e-beam current and/or imparts a chirp to its longitudinal momentum. As the e-beam phase space imprints itself onto the spectrum of emitted photons, all-optical control of electron source enables tailoring the TS γ -ray signal [25, 52].

As explained earlier, the plasma response compresses the optical driver of a conventional LPA (i.e. a transform-limited multi-TW pulse) into a subcycle relativistic optical shock; this happens long before electron dephasing. The shock snowplows the ambient plasma electrons, causing electron density pileup inside the shock and a multifold increase in the field of charge separation behind it [16, 23]. The resulting uncontrolled elongation of the bubble causes massive continuous injection of electrons from its shell. Because of this dark current, caused by the uncompensated adverse optical process, maximization of the energy gain conflicts with the preservation of e-beam quality. We propose to resolve this conflict by incoherently mixing the pulse at the fundamental frequency with a frequency-upshifted pulse of the same, or lower, energy (on a sub-Joule scale) [24, 52]. As the photon diffusion rate due to GVD drops as the frequency grows, the blue-shifted stack component is resilient to self-compression. Because of the strong frequency dependence of the diffusion rate ($\sim \omega^{-3}$) [79], even a modest 25% frequency up-shift appears to be sufficient [24]. Simulations show that even the stack of fully overlapping components, in the fashion of Ref. [80], remains resilient to self-compression (at least on the time scale of electron dephasing). The presence of the almost undeformable blue component does not permit formation of the intensity gradients at the subcycle scale. In the absence of the optical shock, the bubble expansion and, hence the dark current, is insignificant. The particle flux and charge in the energy tail drop multifold in comparison to the reference case of a transform-limited optical driver (the latter complying fully with the scaling (2)). Advancing the blue-shifted component by $T \sim \tau_L$ improves the situation even further. Emulating, in this way, a piecewise, large-bandwidth negative chirp, we essentially place a protective screen ahead of the vulnerable unshifted tail. As this “hard hat” plows through the plasma, expelling background electrons, the soft tail maintains the bubble shape, thus defining kinetics of self-injection. In the regime of our simulations, the dephasing length, defined by the

etching of the head, extends by almost 80%, while the electron energy doubles against the reference case, reaching almost 900 MeV over 2.5 mm acceleration distance. Regardless of the time delay, very quiet injection keeps the e-beam brightness above 4×10^{16} A/m², favoring the use of these beams in Thomson sources [76]. In the case of a time-delayed stack, extracting the e-beam before dephasing (using, for instance, a gas cell target of variable length [81]), thus changing the e-beam energy in the interval 400–900 MeV, preserves its 10^{17} A/m² brightness. This permits the tuning of mean energy of the TS γ -ray signal between 4 and 16 MeV, preserving 1.5×10^6 photons in a microsteradian observation solid angle. Notably, the low energy in the stacked driver (1.4 J) and the ILP (25 mJ) permits maintaining a half-kHz repetition rate while staying below kW average power, a hard yet practical task [77]. A longer ILP would help increase the photon yield by another order of magnitude, without jeopardizing the repetition rate. Overall, this brings an expectation of greater than 10^9 ph/s yield, which is not as high as 10^{13} ph/s permitted by large linacs [57], yet sufficient to identify considerable masses of enriched uranium within minutes [61]. From the viewpoint of laboratory practice, computerized manipulations of the phase and shape of the sub-Joule stack components, using adaptive optics and genetic algorithms [82, 83], should aid greatly in practical realization of the system. This optimization approach is especially effective at a kHz-scale repetition rate and low pulse energy.

The structure of the chapter is as follows: Section 2 describes the computational approach and defines parameters of the case studies. These parameters are representative of LPA experiments carried out in numerous laboratories worldwide. The reported case studies may thus serve as a reference for practical realization of the scheme in an existing experimental setting. In Section 3, we demonstrate the efficiency of using the stacks for generation of low-background electron beams, doubling their energy in comparison with the predictions of accepted scaling laws. Section 4 explores all-optical control over parameters of QME e-bunches, through variation of the time delay between the stack components. A 60% increase in electron energy and a factor 3.5 increase in brightness are demonstrated using the same target and the same energy in the stack. This permits the tuning of the TS γ -ray pulse parameters (mean energy, photon yield, and power) in the broad range of interest for nuclear photonics applications [49]. Section 5 summarizes the results and points out directions for future work.

2. Interaction regimes and simulation methods

Reduced and full 3-D particle-in-cell (PIC) simulations shed light on the physical processes essential for e-beam shaping. Quasistatic simulations using the relativistic, cylindrically symmetric, optical cycle-averaged code WAKE [13, 28] associate the massive dark current with the transformation of the optical driver into an optical shock and help develop a strategy for dark current reduction. WAKE computes the complex envelope of the laser vector potential using an extended paraxial solver. The solver preserves GVD in the presence of large frequency shifts and accurately calculates radiation absorption due to wake excitation [32, 84]. The grid $\Delta\xi \approx \Delta r/3 \approx \lambda_0/13 \approx 63$ nm and time step $\Delta t \approx 1.325/\omega_0$, with 30 macroparticles per radial cell,

are sufficient to capture all physics relevant to pulse propagation and evolution of the bubble. Here, $\xi = z - ct$ and $r^2 = x^2 + y^2$. WAKE includes 3-D test particle tracking in the full (unaveraged) electromagnetic fields. Test-particle simulations allow the study of the physical process of self-injection (bubble and driver evolution) in the absence of effects due to beam loading [21–23]. Simulations using the relativistic, fully explicit, quasicylindrical code CALDER-Circ [85] explore manipulations of e-beam phase space, leading to production of clean and tunable beams. The code uses a numerical Cherenkov-free electromagnetic solver [86] and third-order splines for the macroparticles. These features, in combination with a fine grid $\Delta z = 0.125c/\omega_0 \approx 16 \text{ nm} \approx \Delta r/16$, small time step $\Delta t = 0.1244/\omega_0$, and 45 macroparticles per cell, maintain low sampling noise and negligible numerical dispersion and avoid numerical emittance growth.

We demonstrate the limits of all-optical control fixing the total laser energy at 1.4 J. This energy may be concentrated in a single, transform-limited, linearly polarized Gaussian pulse with a carrier wavelength $\lambda_0 = 0.805 \text{ }\mu\text{m}$ and full width at half-maximum in intensity $\tau_L = 20 \text{ fs}$ (the reference case). The plasma begins at $z = 0$ with a 0.5 mm linear ramp, followed by a uniform section of density $n_0 = 6.5 \times 10^{18} \text{ cm}^{-3}$. The pulse, propagating toward positive z , is focused at the plasma border into a spot $r_0 = 13.6 \text{ }\mu\text{m}$. The electric field in the focal plane is

$$\mathbf{E}_0(x, y, z = 0, t) = \mathbf{e}_x(m_e\omega_0c/|e|)\mathcal{E}_0 \exp(-i\omega_0t - 2\ln 2t^2/\tau_L^2 - r^2/r_0^2) \quad (4)$$

Here, \mathbf{e}_x is the unit polarization vector, and the normalization factor $m_e\omega_0c/|e| = 4 \text{ TV/m}$. The single 70 TW pulse ($\mathcal{E}_0 = 3.27$) has $\tau_L = 2r_m/(3c)$ and thus depletes at the point of electron dephasing, promising to maximize acceleration efficiency. Contrary to expectations, this strategy leads to copious dark current and overall low beam quality. Thus we seek to compensate for the red shift imparted by the wake. This task requires a very broadband negative frequency chirp, that is, blue shifting the leading edge by an amount comparable to the carrier frequency [23–25]. As the required broad-bandwidth, kW average-power laser amplifiers are not going to be available soon [37], we propose to synthesize a large-bandwidth, negative piecewise chirp, by optically mixing transform limited, narrow-bandwidth blocks of the same or different energy [24]. We demonstrate the emerging opportunities by splitting the 1.4 J energy evenly between two linearly (orthogonally) polarized, transform-limited 20 fs pulses, one of which, as shown in **Figure 1(b.1)** and **(c.1)**, is significantly blue-shifted and may be advanced in time. Electric field of this incoherent stack is $\mathbf{E}_{\text{stack}}(z = 0) = \mathbf{E}_0 + \mathbf{E}_{\text{head}}$, with

$$\mathbf{E}_{\text{head}} = \mathbf{e}_y(m_e\omega_0c/|e|)\mathcal{E}_{\text{head}} \exp(-i\omega_{\text{head}}(t + T) - 2 \ln 2(t + T)^2/\tau_L^2 - r^2/r_0^2) \quad (5)$$

Here, $\mathcal{E}_{\text{head}} = \mathcal{E}_0 = 2.31$, \mathbf{e}_y is the unit polarization vector, the delay T is positive, and $\Omega = \omega_{\text{head}}/\omega_0 > 1$. Changing the frequency ratio and the delay permits accessing a broad range of e-beam parameters. We demonstrate the limits of this range by setting $\Omega = 1.5$. (Ref. [24] reports on other options, with equally promising results.) We consider the case of full overlap, $T = 0$ (case A), and then introduce the time delay that maximizes electron energy, $T = 3\tau_L/4 = 15 \text{ fs}$ (case B). **Figure 1** shows that both stacks shrink slowly compared to the reference case, while advancing \mathbf{E}_{head} in time further increases rigidity of the stack.

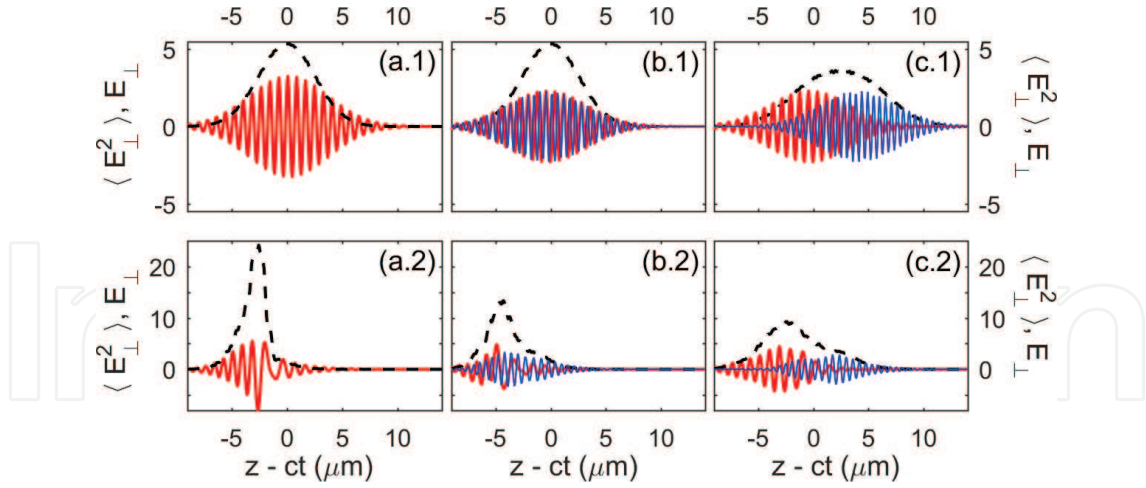


Figure 1. Snapshots of electric field on axis (in units of $m_e \omega_0 c / |e| = 4$ TV/m) show that the frequency shift between stack components makes the stack resilient to self-compression, while the nonzero time delay further increases this resilience. The pulses propagate to the right; $z = ct$ is the centroid of the carrier-frequency component (E_0) in vacuum. Red (thick dark gray): E_0 . Blue (thin gray): E_{head} (in the simulation, $\mathbf{E}_0 \perp \mathbf{E}_{\text{head}}$). Dashed curve: $\langle E_{\perp}^2 \rangle = \langle E_0^2 \rangle + \langle E_{\text{head}}^2 \rangle$, where $\langle \dots \rangle$ denotes averaging over an optical cycle. Panels (a) correspond to the reference case, (b) to case A ($T = 0, \Omega = 1.5$), and (c) to case B ($T = 15$ fs, $\Omega = 1.5$). Top row shows the fields at the plasma entrance ($z = 0$). Bottom row corresponds to (a.2) $z = 1.6$ mm (point of full compression in the reference case), (b.2) and (c.2) $z = 2.15$ mm (dephasing in case A).

To simulate the TS [51], we extract N_b macroparticles from the first and second buckets of the wake and use them to sample the six-dimensional (6-D) phase space of the e-beam. We then propagate a corresponding distribution of non-interacting electrons in free space by solving the relativistic equations of motion. In the absence of a laser field, the trajectories are ballistic. The e-beam collides head-on with the linearly polarized (in the x -direction) interaction laser pulse, which we specify analytically in the paraxial approximation. The ILP has a $0.8 \mu\text{m}$ carrier wavelength (photon energy $E_{\text{int}} = 1.55$ eV), 250 fs duration corresponding to 0.3% FWHM bandwidth in spectral intensity, and a $16.8 \mu\text{m}$ waist size (corresponding to a Rayleigh length of 1.1 mm). Timing between the e-beam and the ILP is such that the centroid of the beam and the peak of the ILP intensity arrive at the ILP focal plane simultaneously. Since in all regimes under consideration the e-beams are relativistic and low-density, $n_e \langle \gamma_e \rangle^{-3} \ll 10^{16} \text{ cm}^{-3}$, space charge forces are negligible [46, 47]. As the energy radiated by an electron passing through the ILP is small if compared to the energy of the electron, the recoil and radiation damping are also negligible. The ILP is shorter than 7% of its Rayleigh length and the e-beam spot size is in the submicron range; hence, the interaction occurs in an almost plane-wave geometry. To avoid broadening the TS spectra [44, 50, 68], a linear interaction regime is chosen, with the ILP normalized vector potential $a_{\text{int}} = 0.1$ (hence the ILP energy 25.5 mJ). Using the computed orbits of individual electrons and taking a weighted average over the ensemble yield the mean energy density radiated per unit frequency ω and solid angle Ω per electron [87]:

$$\frac{d^2 I_e}{d\omega d\Omega} = \frac{e^2 \omega^2}{4\pi^2 c} \left(\sum_{i=1}^{N_b} w_i \right)^{-1} \sum_{i=1}^{N_b} w_i \left| \int_{-\infty}^{\infty} \mathbf{n} \times (\mathbf{n} \times \boldsymbol{\beta}_i) \exp(i\omega(t - \mathbf{n} \cdot \mathbf{r}_i(t)/c)) dt \right|^2 \quad (6)$$

Here, w_i is the macroparticle weight; \mathbf{n} is the unit vector in the direction of observation; and \mathbf{r}_i and $\beta_i = \mathbf{v}_i/c$ are the radius vector and normalized velocity of the electron. A beam with a charge Q radiates the energy $d^2I_{\text{tot}}/d\omega d\Omega = (Q/|e|)d^2I_e/d\omega d\Omega$. In all cases, we show the TS spectra for the emission in the direction of e-beam propagation (on-axis observation).

3. Stacking suppresses dark current

Propagation dynamics of a bi-color stack is entirely different from that of the quasi-monochromatic reference pulse. To track changes in the pulse evolution brought about by the stacking, we use the laser vector potential, $\tilde{a} = a(r, z, \zeta)e^{-i\omega_0\zeta}$, where $\zeta = \xi/c$ is a retarded time, and $a(r, z, \zeta)$ is the complex envelope from WAKE simulations. **Figure 2(b)** and **2(c)** show, for the reference pulse and stack B, the radially integrated mean frequency and frequency variance [88],

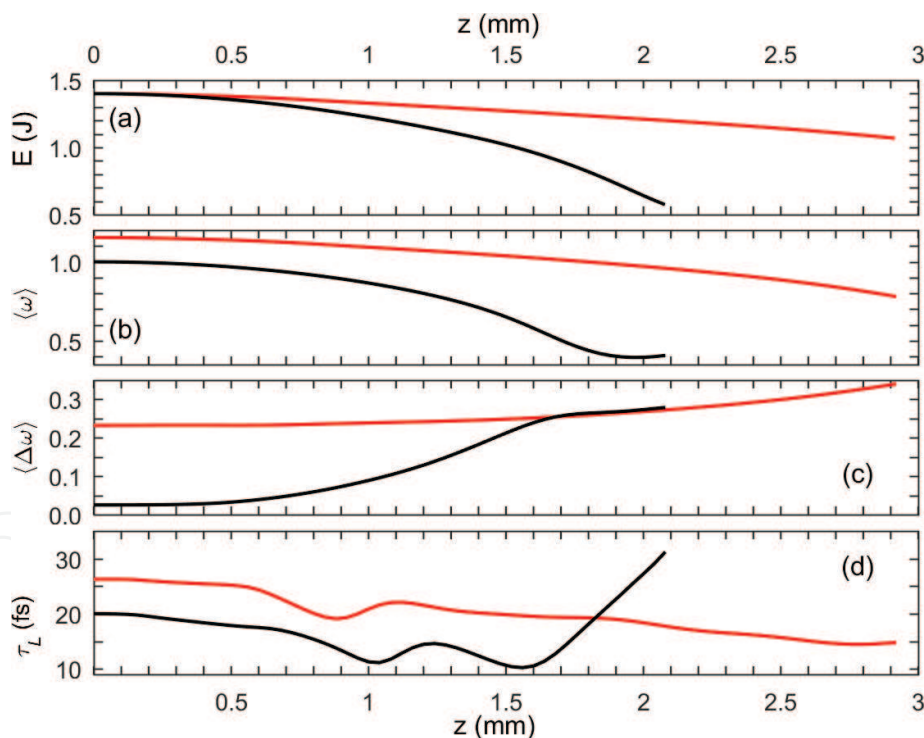


Figure 2. Negative chirp synthesized via pulse stacking mitigates frequency red shift and slows down self-compression (WAKE simulations). The pulses propagate in a uniform plasma toward positive z . Evolution of the (a) pulse energy; (b) mean frequency; (c) frequency variance; and (d) pulse length computed from the ζ -variance of the energy density on axis is shown in the reference case (black) and in case B (red/dark gray). The frequency is in units of ω_0 . The curves terminate as soon as electrons reach dephasing. The negative chirp reduces depletion, red shift, and spectral broadening, thus mitigating contraction of the pulse. Using the stacked driver with a blue component advanced in time (case B) strongly delays dephasing.

$$\langle \omega(z) \rangle = A^{-1} \int_0^{\infty} r dr \omega |\tilde{a}(r, z, \omega)|^2 d\omega, \quad (7)$$

$$\langle \Delta \omega(z)^2 \rangle = A^{-1} \int_0^{\infty} r dr \int_0^{\infty} (\omega - \langle \omega \rangle)^2 |\tilde{a}(r, z, \omega)|^2 d\omega.$$

Here, $\tilde{a}(r, z, \omega) = \int_{-\infty}^{+\infty} \tilde{a}(r, z, \zeta) e^{-i\omega\zeta} d\zeta$ is the Fourier transform of the laser vector potential and $A(z) = \int_0^{\infty} r dr \int_0^{\infty} |\tilde{a}(r, z, \omega)|^2 d\omega$. **Figure 2(d)** shows the mean pulse length computed from the ζ -variance of intensity on axis,

$$\tau_L^2(z) = 8 \ln 2 B^{-1} \int_{-\infty}^{+\infty} (\zeta - \langle \tau \rangle)^2 |a(0, z, \zeta)|^2 d\zeta \quad (8)$$

Here, $\langle \tau(z) \rangle = B^{-1} \int_{-\infty}^{+\infty} \zeta |a(0, z, \zeta)|^2 d\zeta$ is the position of the pulse centroid and $B(z) = \int_{-\infty}^{+\infty} |a(0, z, \zeta)|^2 d\zeta$. **Figure 3** links the local frequency shift to the longitudinal distortion of the pulse. The frequency shift is extracted from the phase of the normalized vector potential, $\tilde{a}(0, z, \zeta) = |a| e^{-i\omega_0\zeta + i\phi}$, using two independent methods [84]. First, the Wigner transform

$$W(\xi, \omega) = \int_{-\infty}^{+\infty} \tilde{a}^* \left(\zeta + \frac{\zeta'}{2}, z \right) \tilde{a} \left(\zeta - \frac{\zeta'}{2}, z \right) e^{i\omega\zeta'} \frac{d\zeta'}{2\pi} \quad (9)$$

yields variation of the “photon density” in time at a given point z on axis. Second, we calculate the instantaneous frequency using the rate of the envelope phase change, $\omega(\zeta) = \omega_0 - d\phi/dt = \omega_0 - \partial\phi/\partial\zeta$. Mean frequency, frequency variance, pulse duration, and photon density are experimentally measurable markers of the nonlinear optical processes. They help identify the regimes of pulse propagation and wakefield excitation [89].

Figure 3(a.1) and **3(b.1)** reveal destruction of the reference pulse at the point of electron dephasing. As the pulse plows through the plasma, it maintains the comoving negative gradient in the nonlinear index of refraction, located at its leading edge [16, 23]. A large local frequency red shift gradually accumulates along the index gradient, eventually exceeding $\omega_0/2$. **Figure 2(a)–(c)** show that, in the process, the energy and mean frequency of the reference pulse drop by 60%, while the mean bandwidth increases 10-fold. The negative GVD of the plasma slows down the red-shifted radiation components, etching away the pulse leading edge. One can clearly see, in the top inset in **Figure 3(b.1)**, the resulting cycle-length optical shock of relativistic intensity. What is more, the photons making up the optical shock keep sliding into the bubble, filling it with the mid-IR radiation at $\omega < \omega_0/4$. Mixing radiation of different frequencies and uncorrelated phases leads to sharp variations in the envelope phase, making the local frequency poorly defined, causing oscillations of the envelope in the tail area. More importantly, the reference pulse fully contracts long before electron dephasing (from 20

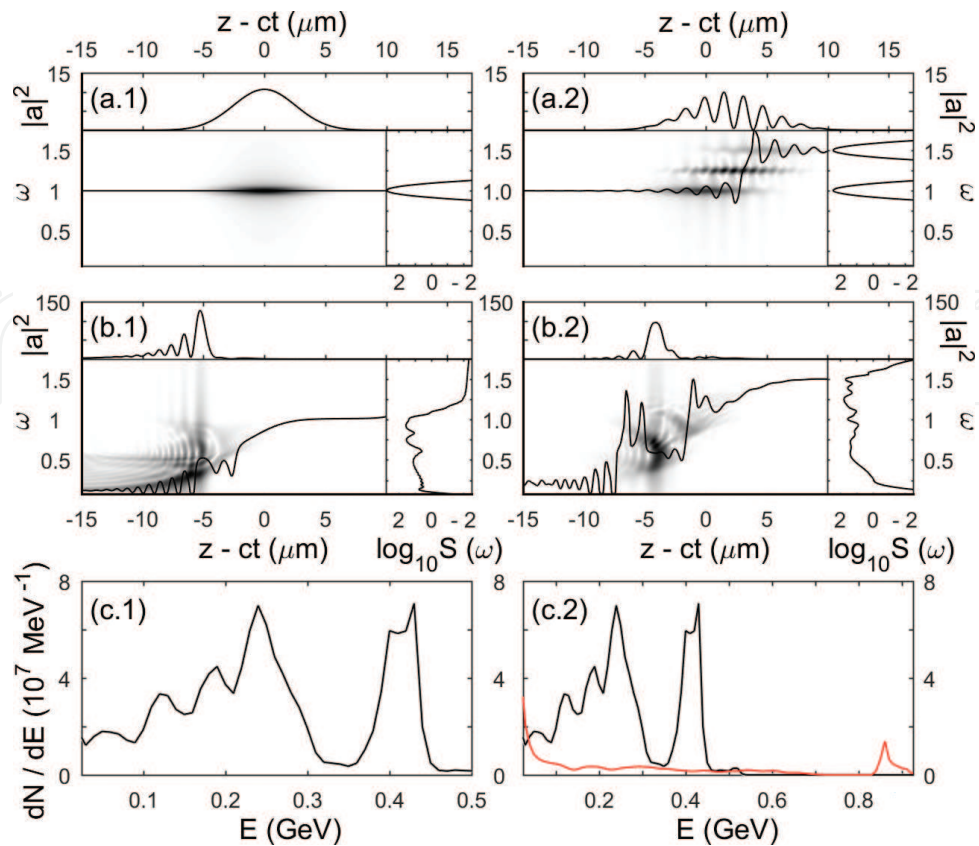


Figure 3. Deformations of the optical driver dictate e-beam quality. Increasing resilience of the driver to self-compression, via negative piecewise chirp imparted by stacking, suppresses the low-energy tail. Left column: Reference case. Right column: Case B ($T = 15$ fs, $\Omega = 1.5$). (a), (b) local frequency shift, spectra, and longitudinal distortion of the pulse from WAKE simulations. The pulse propagates to the right. (a) the pulse at the plasma entrance ($z = 0$) and (b) at the point of electron dephasing ((b.1) $z = 2.03$ mm, (b.2) $z = 3.07$ mm). Grayscale is the absolute value of the Wigner transform (9) in arbitrary units; black curves are lineouts of the instantaneous frequency (in units of ω_0) extracted from the complex pulse envelope. Top inset: normalized intensity on axis. Right inset: radially integrated spectral power, $S(\omega) = \int_0^\infty \omega^2 |a(r, z, \omega)|^2 r dr$, in arbitrary units. (c) Electron spectra at dephasing from CALDER-Circ simulation. Black curves in (c.1) and (c.2) show the reference case spectra ($z = 2.03$ mm). Red (dark gray) in (c.2): Case B ($z = 3.07$ mm). Negative chirp of stack B doubles the energy of the QME signal, while suppressing the flux in the tail by more than an order of magnitude.

to 10 fs, according to **Figure 2(d)** and then almost explosively elongates as newly generated mid-IR radiation slides into the bubble. Continuous injection ensues, building up the massive energy tail shown in **Figure 3(c.1)**, containing three-quarters of the charge accelerated above 50 MeV. CALDER-Circ simulation corroborates and adds more details to this unfavorable scenario. **Figure 4** links self-injection to the bubble evolution. The bubble size (shown in (a)) is defined as the length of the accelerating phase on axis (i.e. the length of the region inside the bubble where the longitudinal electric field is negative). Panel (b) tracks accumulation of the charge in the first two buckets, counting only electrons with $E > 50$ MeV. The collection phase space (longitudinal momenta of electrons at dephasing vs. their initial positions, (c)) and collection volume (initial positions of electrons with $E > 50$ MeV at dephasing, (e)) parameterize the energy gain of electrons with their initial coordinates. As the reference pulse adjusts for self-guiding, its spot size oscillates at least once. **Figure 4(a)** shows that it is during this early

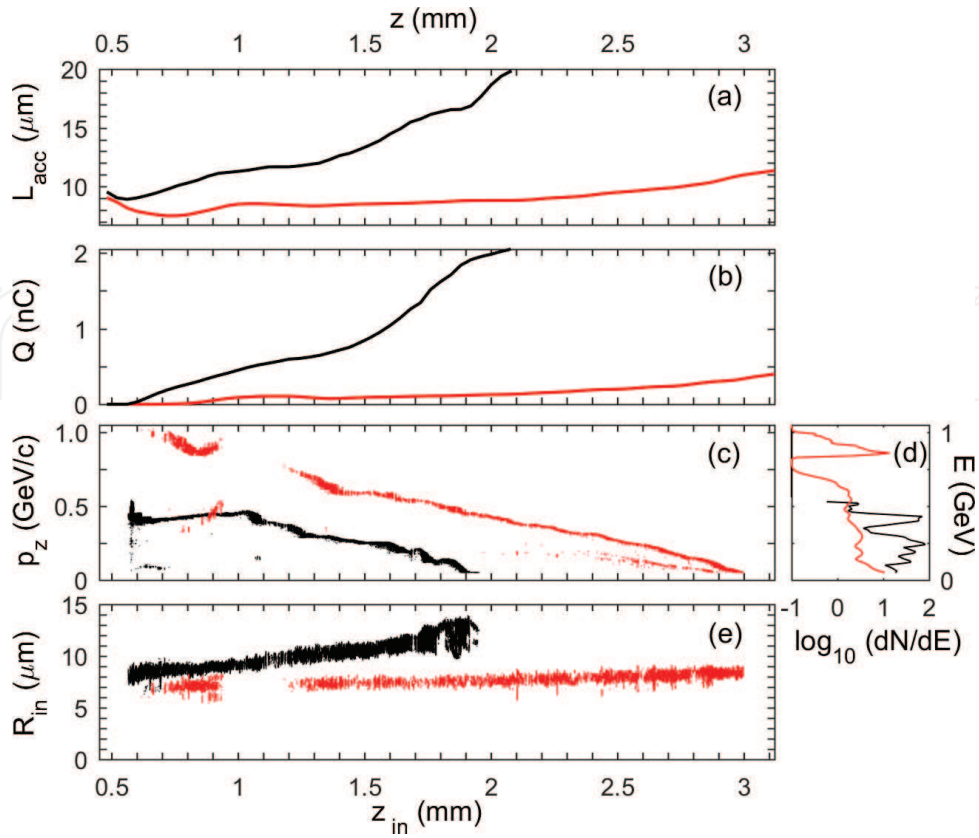


Figure 4. Stacking reduces expansion of the bubble, suppressing the dark current, avoiding the buildup of a low-energy tail in electron spectra (CALDER-Circ simulations). Black: the reference case. Red/dark gray: case B. (a) Length of the accelerating phase on axis vs. propagation length. (b) Charge accelerated in the first two buckets. (c) Longitudinal collection phase space of electrons from the first two buckets. (d) Energy spectra. These are identical to those in **Figure 3** (c.2), yet shown on a logarithmic scale, to evaluate suppression of the tail. (e) Collection volume. Data in plots (c)–(e) correspond to electron dephasing, $z = 2.03$ mm in the reference case and 3.07 mm in case B. The piecewise negative chirp of the stacked driver suppresses expansion of the bubble, reducing the flux in the energy tail by more than an order of magnitude, while doubling the energy of QME component.

stage (between $z \approx 0.55$ and 1.3 mm) that the bubble expands, injecting electrons, and then stabilizes, forming the QME bunch. Self-compression of the pulse starts early. As the optical shock builds up, the bubble starts to expand. Explosive expansion after $z \approx 1.3$ mm, with an almost 65% increase in size by the dephasing point ($z = 2.03$ mm), adds an extra 1.25 nC to the energy tail (in effect, multiplying the tail charge by a factor of 6). Beam loading saturates injection near dephasing, eventually destroying the bubble.

Figure 3(a.2)–(c.2) shows that the piecewise negative chirp turns the tide, enabling acceleration through dephasing without sacrificing e-beam quality. As a collateral benefit, electron energy doubles against the scaling-prescribed limit of the reference case. **Figure 4(c)** shows that, in case B, the injection starts later than in the reference case, while the bucket contracts rather than stabilizes around $z \approx 1.3$ mm, expelling one-third of the earlier injected charge. This reduces the bunch charge by a factor 8 in comparison with the reference case. Yet, from the data in **Table 1**, this reduction comes from clipping the bunch, from 5.5 fs to less than a femtosecond, with the average current preserved (≈ 88 kA). As soon as the QME bunch forms, the resilience of the stack to self-compression keeps it almost background-free (cf. **Figures 3(c.2)**

Parameter (unit)	$\langle z \rangle$ (mm)	Q (pC)	$\langle E \rangle$ (MeV)	σ_E (MeV)	σ_τ (fs)	σ_α (mrad)	ϵ_\perp^n (mm mrad)	$\langle I \rangle$ (kA)	B_n (A m ⁻²)	W (mJ)
QME bunches										
Reference	2.027	493.5	426.5	25.7	5.5	2.93	0.69	89.7	0.38×10^{17}	210.4
Case A	2.148	288.8	524.8	26.3	3.8	2.75	0.64	76.2	0.38×10^{17}	151.5
Case B	1.473	73.8	442.9	31.8	0.85	2.16	0.3994	87.3	1.1×10^{17}	32.7
Case B, dephasing	3.067	73.8	881.9	28.6	0.85	1.35	0.3994	87.3	1.1×10^{17}	65.1
Energy tails ($E > 50$ MeV)										
Reference	2.017	1454	212.9	67.0	11.0	9.0	—	132	—	309.5
Case A	2.1425	363.3	253.2	113.4	5.5	6.52	—	66.1	—	91.2
Case B	1.4735	27.55	114.7	43.25	0.33	4.15	—	82.7	—	3.2
Case B, dephasing	3.062	329.8	298.4	174.6	8.84	5.16	—	37.3	—	98.4

Only particles from the first bucket are included. $\langle z \rangle$ is a longitudinal position of the beam centroid; Q is the charge; $\langle E \rangle$ is the mean energy; σ_E is the energy variance; σ_τ is the root-mean-square bunch length; σ_α is the root-mean-square divergence; ϵ_\perp^n is the root-mean-square normalized transverse emittance; $\langle I \rangle = Q/\sigma_\tau$ is the average current; B_n is the 5-D brightness; W is the total energy of the bunch.

Table 1. Electron beam statistics.

and **4(d)**). In summary, stacking changes the system dynamics as follows. First, per **Figure 2(a)**, the pulse energy loss is merely one-quarter, in stark contrast with 60% of the reference case. Second, as is seen in **Figure 2(d)**, the stack reaches full compression at the point of electron dephasing rather than halfway through. **Figure 3(b.2)** shows that the energy of the stacked driver finally concentrates in a spike 2.5 optical cycles long, with the instantaneous frequency almost uniform along the pulse body. There is no sign of photon phase space rotation, with a mid-IR tail protruding into the bubble, nor there is a signature of a subcycle rising edge (the key feature of the reference scenario). Hence, the electron density pileup inside the compressed stack is minimal (cf. Figure 6 of Ref. [24]). Thereby, the resulting 7-fold reduction in the bubble expansion rate, evaluated from **Figure 4(a)**, reduces the average flux in the tail by a factor of 16 and the charge by a factor of 6. The QME peak dominates the electron spectrum, having the mean energy twice as high, and 5-D brightness a factor of 3.3 higher than its reference counterpart. Notably, the boost in energy has little to do with beam loading. As mentioned earlier, the current density in the QME bunches (the key factor defining the effect [26]) is almost the same in both cases. As expected, the WAKE test particle simulations show that the beam loading reduces electron energy by 25% in the reference case and merely by a few percent in case B. Hence, three-quarters of the observed energy boost are due to the favorable changes in the driver dynamics and quasistatic plasma response brought about by photon engineering.

Collection volume presented in **Figure 4(e)** indicates that only electrons with initial radial positions such as those that enter the bubble sheath are trapped and accelerated. There is no sign of transient injection from the near-axis region. The injection candidates fill a thin

cylindrical shell with a radius slightly smaller than the bubble radius, accurately reproducing evolution of the pulse spot size in the cross-section at the highest intensity, which agrees with the matching condition (1). Indeed, for the 70 TW, 20 fs reference pulse, the power ratio $P/P_{\text{cr}} = 16.25$ yields the matched spot $r_m \approx 9.4 \mu\text{m}$. The collection radius in **Figure 4(e)** varies by $\pm 1 \mu\text{m}$ from this value through 70% of the acceleration distance. The dephasing length, calculated with this r_m , is $L_d \approx 1.65 \text{ mm}$, which is within 10% of the value estimated from **Figure 4(e)** (black markers). The estimated energy gain (2) is 430 MeV, nearly the same as the simulated $\langle E \rangle \approx 426.5 \text{ MeV}$. Thus, the QME bunch of the reference scenario complies with the scaling predictions exceptionally well. Yet, accumulation of the low-energy tail ruins the beam by the end of acceleration.

In case B, slow self-compression of the rigid head delays dephasing. Applying the scaling formulae to the 35 TW, 20 fs head with the wavelength $\lambda_{\text{head}} = (2/3)\lambda_0 \approx 0.533 \mu\text{m}$ (so that $P/P_{\text{cr}} \approx 3.6$), we find $r_m \approx 7.3 \mu\text{m}$. Again, this value of r_m deviates from the collection radius shown in **Figure 4(e)** (red markers) by less than $\pm 1 \mu\text{m}$ throughout the entire interaction. The estimated dephasing length, $L_d \approx 2.95 \text{ mm}$, is 15% longer than that obtained in the CALDER-Circ simulation. At the same time, the estimate of the energy gain at dephasing (using a generic formula (5) of Ref. [18]) is only 630 MeV, which is 30% lower than the gain obtained in the CALDER-Circ simulation with a bi-color stack. Even though, according to the scaling, using the head alone should boost electron energy effectively, the presence of the unshifted tail is important. As the rigid head of the stack plows through the plasma, driving the wake, the flapping of the slightly mismatched tail inside a soft channel (electron density bubble) controls the bubble radius, thus determining kinetics of self-injection [25]. The presence of the tail is thus essential to maintain sufficiently high charge (or modulate the beam current [25]). Since the tail rides inside the bubble devoid of electrons, it remains uncompressed. As the head starts experiencing red shift, the GVD-delayed red-shifted radiation superimposes onto the smooth profile of the tail. The combination of the two does not permit formation of a subcycle rising edge (compare **Figure 3(b.1)** and **3(b.2)**), which avoids uncontrollable expansion of the bubble.

Table 1 quantitatively assesses improvements in e-beam quality, showing parameters of QME bunches and energy tails at dephasing. Statistics of case B are complemented with the data taken at the point where the bunch energy matches the energy gain in the reference case ($E \approx 430 \text{ MeV}$, $z \approx 1.47 \text{ mm}$). **Table 1** presents the metrics that are essential to evaluate the 5-D brightness, $B_n = 2\langle I \rangle (\pi \varepsilon_{\perp}^n)^{-2}$, the quantity defining a capability of the beam to drive a TS-based γ -ray source [76]. Here, $\langle I \rangle = Q/\sigma_{\tau}$ is the mean current; Q is the bunch charge; σ_{τ} is the root-mean-square bunch length; and $\varepsilon_{\perp}^n = 2^{-1/2} \left((\varepsilon_x^n)^2 + (\varepsilon_y^n)^2 \right)^{1/2}$, where $\varepsilon_i^n = (m_e c)^{-1} \left((\langle p_i^2 \rangle - \langle p_i \rangle^2) (\langle r_i^2 \rangle - \langle r_i \rangle^2) - (\langle p_i r_i \rangle - \langle p_i \rangle \langle r_i \rangle)^2 \right)^{1/2}$ is the root-mean-square normalized transverse emittance. Statistics for case B show that the QME bunch progresses through dephasing with the normalized transverse emittance conserved, as should be the case for the adiabatically slowly varying structure. Simulating e-beam dynamics, while conserving the emittance better than in the fourth digit, became possible due to elimination of the numerical Cherenkov radiation [86] in CALDER-Circ. Any degradation of the Thomson γ -ray signal observed in the simulations must be thus attributed to the physical causes rather than to numerical artifacts. The QME bunch B,

apart from 3.2% energy spread, sub-fs duration, and 400 nm emittance (about half of that of the reference case), has the 5-D brightness 1.1×10^{17} A/m², preserved throughout acceleration. This is most encouraging for using the beam as a driver of a high-flux Thomson source [76].

4. Stack-driven electron beams generate high-flux, femtosecond γ -ray pulses via Thomson scattering

The capability of a stack-driven LPA to suppress the low-energy background and to increase electron energy gain, while preserving 100-pC scale charge and 100-kA average current, boosting the e-beam brightness beyond 10^{17} A/m², is an asset for the design of radiation sources.

4.1. Improving performance of the γ -ray source: suppressing emission of low-energy photons and boosting the energy of quasi-monochromatic signal

A broadband e-beam accelerated with a transform-limited pulse is poorly suited to produce quasi-monochromatic γ -ray pulse via the TS mechanism. **Figure 5(a)** demonstrates the phase space of the e-beam at dephasing, with a QME component accompanied with a massive energy tail. We separate the macroparticles making up the QME e-bunch and the tail, as shown in **Figure 5(a)**, and carry out two sets of TS simulations with these initial conditions. The partial photon spectra displayed in **Figure 5(c)** reveal modest energy of γ -photons emitted by the

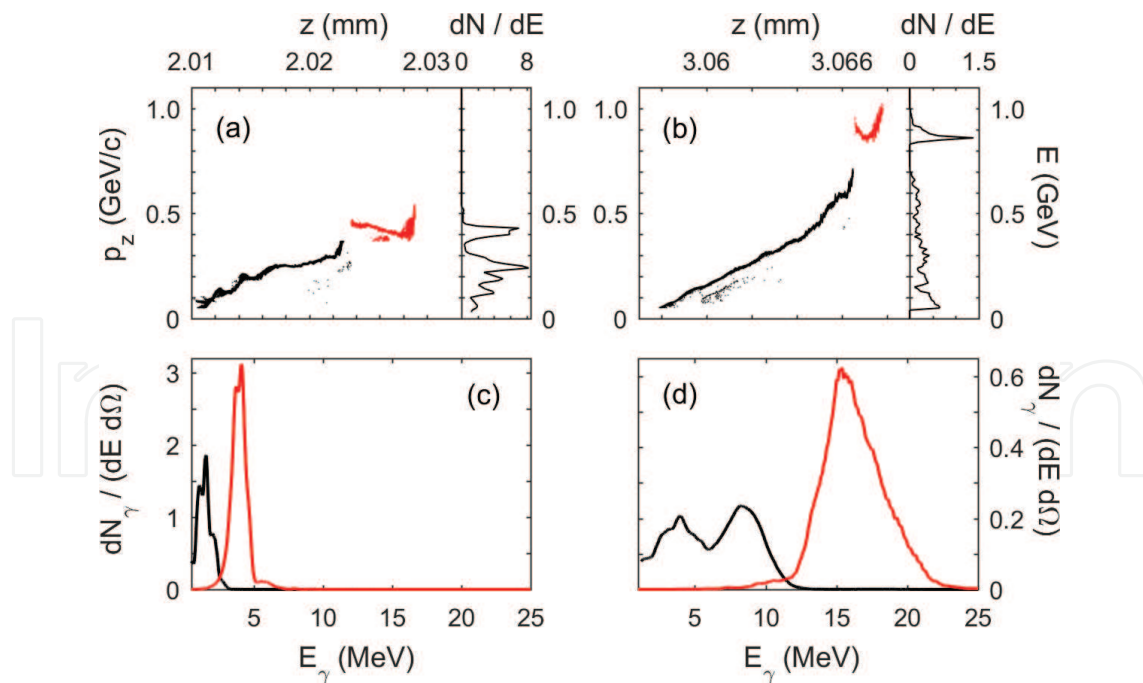


Figure 5. The stack-driven LPA delivers a low-background QME electron bunch. Thomson scattering from this bunch produces a quasi-monochromatic, sub-fs γ -ray pulse. Electron beams are extracted from CALDER-Circ simulations at dephasing. (a), (c) reference case. (b), (d) case B. (a), (b) longitudinal phase space of the bunch; inset: energy spectrum (in units MeV⁻¹). (c), (d) γ -ray flux in the direction of e-beam propagation (in units 10^{12} MeV⁻¹ sr⁻¹). QME components of e-beams and corresponding quasi-monochromatic components of γ -ray pulses are depicted in red (dark gray).

QME bunch in the direction of its propagation, $\langle E_\gamma \rangle \approx 3.85$ MeV. This is too low to meet the needs of nondestructive inspection systems for special nuclear materials; these require photon energy tunable in the range 5–15 MeV [49]. **Figure 5(c)** reveals a rather high ratio of noise to the quasi-monochromatic signal, 1:2, on average. Conversely, the virtual lack of the low-energy background in case B favorably reflects on the TS signal. The latter, from **Figure 5(d)**, has an average noise-to-signal ratio twice as low, 1:4, and nearly a factor 4 higher mean photon energy, $\langle E_\gamma \rangle \approx 16$ MeV. Yet, the signal bandwidth is rather high, 15.7%.

From a single-particle theory [50], both variation in energy of an electron and a misalignment of its trajectory with the propagation axis of the ILP tend to reduce the photon energy, thus contributing to the photon energy spread. The QME bunch of case B, apart from having a 3.2% energy spread, has a rather high root-mean-square divergence, $\sigma_\alpha = 1.35$ mrad, or $2.33\langle\gamma_e\rangle^{-1}$.

Here, $\langle\gamma_e\rangle$ is the mean Lorentz factor of the bunch, and $\sigma_\alpha = 2^{-1/2}\left(\sigma_x^2(\alpha) + \sigma_y^2(\alpha)\right)^{1/2}$, where $\sigma_i(\alpha) = \langle p_z \rangle^{-1} \left(\langle p_i^2 \rangle - \langle p_i \rangle^2 \right)^{1/2}$.

TS simulations with the reduced phase space of e-beam help identify the primary contributor to the photon energy spread. First, we plot in **Figure 6** (black in both panels) the spectrum of γ -photons emitted by the bunch with a complete 6-D phase space (the region of phase space depicted with red/dark gray markers in **Figure 5(b)**). The signal with a 15.7% energy spread is centered at $\langle E_\gamma \rangle = 16$ MeV. Then, transverse momenta of all macroparticles are set to zero, while their longitudinal momenta, p_z , are unchanged. This preserves the energy spread while zeroing out the divergence. Lastly, $p_z = \langle p_z \rangle = 1725.8m_e c$ is assigned to all electrons, while p_x and p_y are unchanged. This preserves mrad-scale divergence of the bunch, while nearly zeroing out the energy spread. In the zero-divergence case (spectrum depicted in red/dark gray in **Figure 6(a)**), the mean photon energy increases to 18 MeV, while the energy spread stays at 12.8%. In stark contrast, the case with a near-zero energy spread yields a TS signal with a *subpercent* energy spread, centered at $E_\gamma \approx 4\langle\gamma_e\rangle^2 E_{\text{int}} \approx 18.4$ MeV (red/dark gray in **Figure 6(b)**). Thus, the γ -ray signal receives its large (more than 10%) bandwidth almost entirely from a few-percent electron energy spread. Further steps in optimization of the LPA should aim to

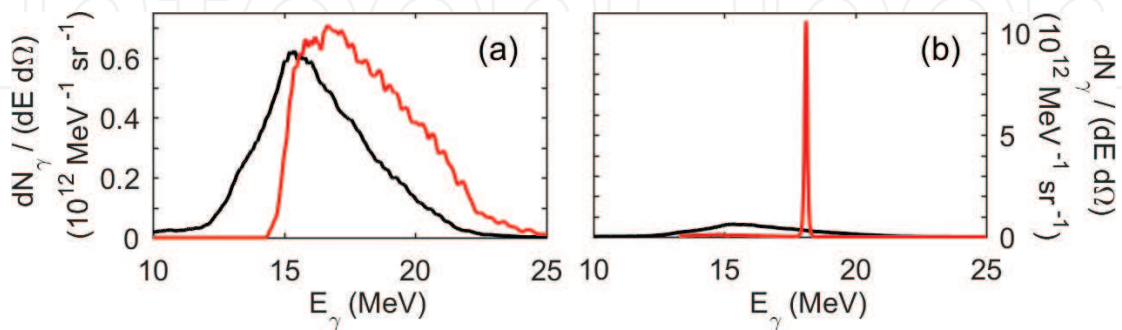


Figure 6. Energy spread in the electron bunch determines the energy spread of emitted γ -photons. Black: TS spectrum from the simulation using complete phase space of electron bunch (same as red (dark gray) in **Figure 5(c)** and **5(d)**). Red (dark gray): simulations with the reduced phase space of electrons, with (a) zero dispersion of transverse momentum (zero divergence) and (b) zero dispersion of longitudinal momentum (viz. almost vanishing energy spread).

reduce the energy spread below 1%. One practical way to do it (at the expense of reduction in charge and, hence, brightness) is to select electrons from narrow energy intervals within the e-beam bandwidth by selective focusing with highly chromatic magnetic quadrupole lenses [90] before the collision of e-beam with the ILP. (At the same time, the magnetic quadrupole will disperse the residual energy tail.)

The collimation of high-energy γ -photons and the number of photons in the observation cone are important metrics for applications. To evaluate the reduction in photon energy and flux with an increase in the observation angle (viz. to estimate the effective apex angle of the photon emission cone), we select the macroparticles making up the QME e-bunch and carry out the TS simulation with these initial conditions. We detect the photons scattered in and out of the ILS polarization plane, in the direction of e-beam propagation ($\theta = 0$) and at small angles measured from the direction of e-beam propagation, up to the root-mean-square divergence angle, $\theta = \sigma_\alpha = 2.33\langle\gamma_e\rangle^{-1}$. As the scattering angle increases to $\theta = \langle\gamma_e\rangle^{-1}$, the mean photon energy drops by 25%, the energy spread staying at the 15–20% level. At the same time, the photon flux drops 10-fold. To a good approximation, there are virtually no photons with the energies above 10 MeV outside the observation cone of apex angle $2\theta = 2\langle\gamma_e\rangle^{-1}$. Thus, to estimate the number of QME high-energy photons scattered in the direction of e-beam propagation, we choose conservatively the observation solid angle $\Delta\Omega_\gamma = (\pi/2)\langle\gamma_e\rangle^{-2}$, that is, the solid angle of the cone with an apex angle $2\theta = \sqrt{2}\langle\gamma_e\rangle^{-1}$ ($\approx 2 \times 0.69$ (2×0.41) mrad for the beam A(B) at dephasing). We take the photon flux corresponding to the direct backscattering ($\theta = 0$), integrate it over the energy, and multiply the result by $\Delta\Omega_\gamma$.

Table 2 presents statistics of quasi-monochromatic γ -ray signals corresponding to the QME entries in **Table 1**. The entries corresponding to the beam B show the photon yield over 1.5×10^6 per pulse. This is comparable to the experimental yields with 100-MeV scale e-beams, 3×10^5 to 10^7 [66, 67, 70], calculated for the entire forward hemisphere, and integrated over the entire broad bandwidth of the γ -ray beam. Yet, our highest-energy photons reach 16 MeV while preserving a 16% energy spread and microsteradian collimation, which is strikingly better than 50–100% spread and millisteradian collimation reported for the sub-MeV photons [66, 67, 70].

Parameter	$\langle E_\gamma \rangle$ (MeV)	σ_E (MeV)	$\Delta\Omega_\gamma$ (μsr)	N_γ (10^6)	W_γ (μJ)
Reference	3.85	0.72	2.25	8.95	5.5
Case A	5.67	0.97	1.49	5.08	4.6
Case B	4.36	0.93	2.09	1.52	1.1
Case B, dephasing	16.0	2.51	0.53	1.58	4.0

Corresponding energy spectra are depicted in **Figure 5(c)** (reference); **Figure 7(c)** (case A); **Figure 7(d)**, red (case B before dephasing); and **Figure 7(d)**, black (Case B at dephasing). $\langle E_\gamma \rangle$ is the mean energy; σ_E is the energy variance; N_γ and $W_\gamma = N_\gamma\langle E_\gamma \rangle$ are the number of photons and energy radiated into the observation solid angle $\Delta\Omega_\gamma = (\pi/2)\langle\gamma_e\rangle^{-2}$ in the direction of e-beam propagation.

Table 2. Statistics of γ -rays emitted by the QME bunches with parameters from **Table 1**.

4.2. Tuning the energy and flux of the quasi-monochromatic γ -ray signal

The structure of e-beam phase space is sensitive to variations in the drive pulse evolution brought about by changes in the initial conditions. This responsiveness improves parameters of the beam to make it suitable to drive a quasi-monochromatic radiation source based on Thomson scattering, a process demanding exceptional beam quality. **Figure 7** displays the capability of the all-optical Thomson source to produce γ -ray pulses with different characteristics (such as a mean energy and flux) while maintaining high yield and low background. This flexibility is demonstrated without changing the energy of the stack or the frequency ratio between its components. This is an asset to applications, which often need to adjust to new conditions in a timely fashion, avoiding a major upgrade of the laboratory.

Changing the e-beam energy, while keeping the brightness fixed, is one option offered by case B. Standard targets, such as printed gas cells of variable length [81], permit the necessary reductions in the plasma length. **Figure 7(b)** shows progress of the e-beam through dephasing, from the energy matching the maximal gain in the reference case (≈ 430 MeV) to 882 MeV. Notably, the QME bunch reaches dephasing, while maintaining $B_n = 1.1 \times 10^{17}$ A/m². This conserves the number of photons emitted into the μ sr-scale detection angle, $N_\gamma \approx 1.55 \times 10^6$. Thus, a quasi-monochromatic (15.7–21.3% energy variance) 0.85 fs γ -ray pulse with the mean energy tunable between 4 and 16 MeV (1.3–4.7 GW average power) can be produced.

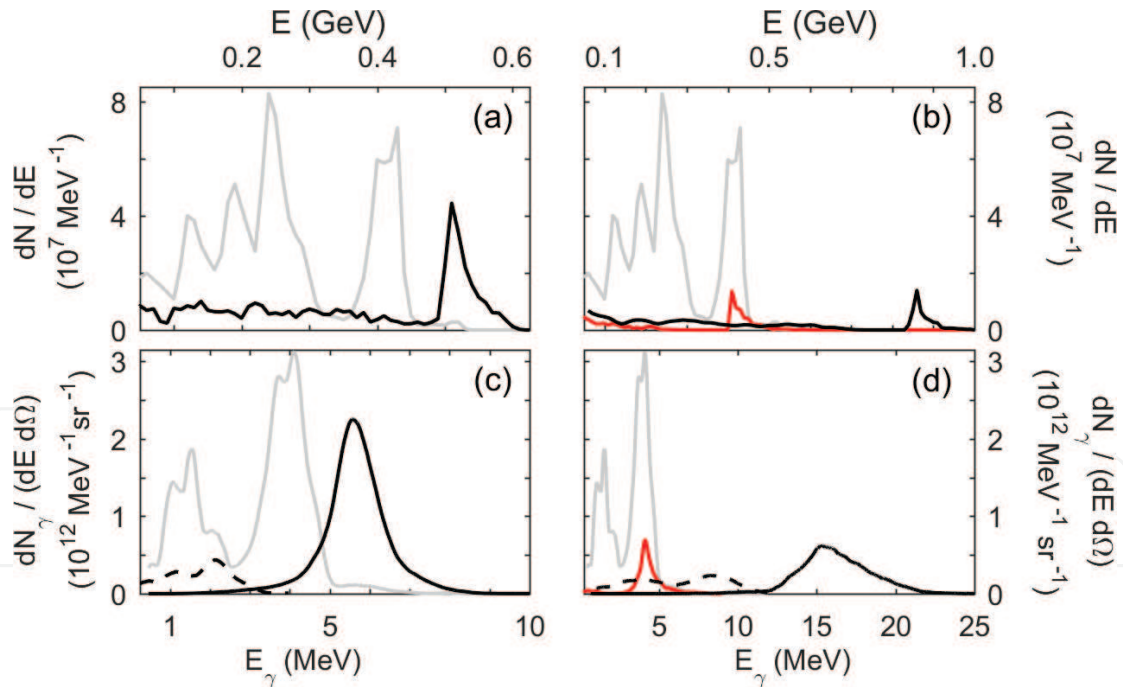


Figure 7. The stack with fully overlapped components (case A, panels (a), (c)) preserves high electron and γ -ray flux similar to that of the reference case, while suppressing the background. The stack with a blue component advanced in time (case B, panels (b), (d)) permits doubling electron energy against the reference case, increasing the photon energy by a factor 3 in comparison to case A, at the expense of reduction in flux. (a), (b) electron energy spectra. (c), (d) spectra of γ -photons emitted in the direction of e-beam propagation. Gray: Spectra of the reference case. Black: electron and photon spectra corresponding to e-beams extracted at dephasing ($z \approx 2.15$ mm, case A; $z \approx 3.07$ mm, case B). Dashed curves in (c) and (d): spectra of photons emitted by the electron energy tails. Red (dark gray): E-beam of case B, extracted prior to dephasing, $z \approx 1.47$ mm.

Reducing the time delay between stack components increases photon yield at relatively low energies ($\langle E_\gamma \rangle \leq 10$ MeV), the ultimate example of which is case A (full overlap). The physical difference between cases A and B is remarkable. Stack A is an incoherent mix in the fashion of Ref. [80] rather than a pulse with a negative piecewise chirp. As the stack A components plow through the plasma, they both ride on the down-slope of the nonlinear index, such as depicted, e.g. in **Figure 7** of Ref. [16] or **Figure 5** of Ref. [22]. From **Figure 1(b.2)**, the frequency unshifted component, E_0 , red-shifts and compresses to nearly a single cycle, in the same fashion as the reference pulse does (cf. **Figure 1(a.2)**). At the same time, the blue-shifted E_{head} remains virtually intact. **Figure 1(b.2)** also shows that the stack components stay together, accumulating merely a two-cycle delay due to the difference in their group velocities. The stack thus does not break up longitudinally. The superposition of compressed E_0 and almost intact E_{head} does not allow for the formation of a subcycle rising edge (optical shock) such as develops in the reference case (**Figure 1(a.2)**). The undelayed E_{head} is thus akin to a rigid exoskeleton protecting the vulnerable E_0 .

Deformation of a stack with fully overlapped components, the process that defines the dephasing length [18], is dominated by rapid self-compression of the least resilient stack component, E_0 . As E_0 self-compresses (and hence, the stack self-compresses) at the same rate as the drive pulse in the reference scenario, the dephasing length remains almost unchanged, and the boost in electron energy (by 23%) is unremarkable. **Table 1** shows that the QME bunch of case A is not very different from its reference counterpart (note that their 5-D brightness is the same.) Conversely, the electron energy tail in case A is suppressed, with a factor 4 reduction in charge and 7 in average flux. This drastically improves the noise-to-signal ratio of emitted γ -rays, from roughly 1:2 in the reference case to better than 1:5 in case A, as may be evaluated from photon spectra in **Figure 7(c)**. **Table 2** shows that the γ -ray pulse, in case A, contains about 5×10^6 photons, a factor 3.3 higher yield than in case B. Further, these photons receive 50% boost in energy with respect to the reference case². Changing the time delay between the stack components is thus a proper way to control the TS photon yield and energy.

4.3. Final notes on all-optical control of quasi-monochromatic Thomson sources

The results presented above offer an opportunity for tuning the γ -ray energy and flux in a broad range, without changing the total (Joule-per-pulse) laser energy in the LPA.

Particularly, the interval of photon energy variation, 4–16 MeV, with the yield $(1.5 - 5) \times 10^6$ photons per pulse, meets the needs of nuclear photonics applications [49]. Raising the photon yield per second is technologically possible. Using a longer (up to 2.5 ps) ILP with the same spot size and amplitude ($a_{\text{int}} = 0.1$) may increase the yield by up to an order of magnitude. This long ILP is still shorter than its half-Rayleigh length. This is sufficient to preserve the nearly plane-wave character of the interaction with the e-bunch. As the energy (0.25 J) of the long ILP is still below the stack energy (1.4 J), their repetition rates may be matched. Then, using a kW-scale laser amplifier [77] permits the production of Joule scale pulses (LPA stack

²Increasing the ILP frequency may substantially increase the photon energy, while preserving the high flux [72].

and ILP) at a few hundred Hz, increasing the photon yield beyond 10^9 ph/s. Apart from keeping the photon yield at a competitive level, this repetition rate permits real time optimization of the experiment [82, 83], not possible with one shot per hour PW facilities [73].

The estimated 10^9 ph/s yield is sufficiently high to make the tunable TS source interesting for the design of a nondestructive inspection system for special nuclear materials. Simulations, based on data from recent detection experiment [61], indicate that the TS γ -ray flux of 10^6 ph/s, with a 5% signal bandwidth and a 10 Hz repetition rate, is sufficient to identify a nuclear resonance fluorescence peak from a 1 kg of highly enriched uranium within 10 minutes. The higher flux accessible with our source would compensate for its still significant (up to 20%) bandwidth. Alternatively, frequency chirping of the ILP may reduce the photon energy spread [51]. Given the unconventional U-shape of electron momentum chirp in the QME e-bunch (cf. **Figure 5(a)** and **5(b)**), this topic deserves special consideration but is beyond the scope of this chapter.

Lastly, e-beam optimization studies, using stacks with different frequency ratios [24], show that, as long as the time delay and energy partition between the stack components are fixed, and $\Omega \geq 1.25$, the electron energy gain is quite insensitive to the frequency ratio. Even though the particle flux dN/dE in the QME bunch drops as $\Omega \rightarrow 2$, reducing the quasi-monochromatic γ -ray yield, the TS signal still has a quality far exceeding that accessible in the reference scenario. This observation permits a considerable technological flexibility in a practical realization of this concept. Frequency shifting on the modest scale ($\Omega \leq 1.5$) can be accomplished with a Raman cell, with subsequent conventional chirped-pulse amplification [91–93]. Alternatively, energy-efficient methods of frequency doubling may be applied.

5. Summary and outlook

In a conventional LPA, a cavity of electron density maintained by the radiation pressure of a single narrow-bandwidth laser pulse accelerates electrons self-injected from the ambient plasma. Deformations of the bucket, which carry on in lock-step with the deformations of the optical driver, determine the structure of the e-beam phase space. Optimizing the nonlinear evolution of the drive pulse is an essential element of LPA design, offering new avenues to coherently control e-beam phase space on the femtosecond scale.

Compact sources of quasi-monochromatic γ -photons, based on the TS mechanism, are highly sensitive to the quality and phase space structure of the driving GeV-scale e-beams. Reaching sufficient e-beam brightness and energy, while maintaining a modest facility footprint and high repetition rate, is a major challenge for a traditional LPA. The first roadblock is the limit on electron energy imposed by dephasing, with unavoidable beam contamination with a low-energy background, while the second is the low repetition rate of petawatt-scale lasers (which limits the dosage, frustrating applications). Reducing the energy in the drive pulse to a sub-Joule level may alleviate the latter, yet aggravating the former. Our simulations show the way to resolve this conflict, by synthesizing the LPA drive pulse by incoherently stacking collinearly propagating 10-TW-scale pulses of different wavelengths. Stacking introduces a frequency bandwidth sufficient to compensate the red shift imparted by the wake excitation.

Unlike a single, transform-limited pulse, the stack is nearly immune to degradation while driving the bubble in a dense plasma ($n_0 \sim 10^{19} \text{ cm}^{-3}$). Advancing the blue-shifted component of the stack in time emulates the negative frequency chirp [16, 23–25]. This delays dephasing of the electrons, doubling their energy compared to the scaling predictions, using no manipulations of a few mm-length gas target. Importantly, immunity of the stacked driver to self-compression keeps the low-energy electron flux so modest as to almost avoid contamination of TS γ -ray pulse with low-energy photons.

Simulation data presented here show that increasing the delay between the stack components, while keeping the same total laser energy and frequency ratio, permits increasing electron energy from 525 to 900 MeV, boosting the 5-D brightness nearly three-fold. This puts generation of 10 MeV-scale, few-GW, quasi-monochromatic, femtosecond-length γ -ray pulses via Thomson scattering within reach of existing laser technology. Energy of these pulses, containing up to 5×10^6 photons into the microsteradian cone, may be tuned in the range 4–16 MeV and, possibly, beyond, while the low-energy photon background remains insignificant. Increasing the LPA repetition rate to kHz level, at affordable average power, promises boosting photon yield beyond 10^9 ph/s, making tunable, all-optical TS γ -ray sources interesting for applications [48, 49, 61]. As a further development, focusing the stack components differently [52], or propagating the stack in a channel [24, 25], enables generation of a train of GeV-scale, ultrabright electron bunches with a femtosecond synchronization. These unconventional comb-like e-beams may emit polychromatic trains of high-flux γ -ray pulses consisting of a few distinct energy bands, in the range 3–17 MeV [52]. The natural mutual synchronization of fs-length e-bunches and γ -ray pulses may be an asset to nuclear pump-probe experiments. With a γ -ray beam spectrally resolved, each beamlet may give a “movie frame” on a femtosecond time scale to image ultrafast phenomena in a dense matter [74].

Acknowledgements

The US DOE Grant DE-SC0008382 and National Science Foundation Grants PHY-1104683 and PHY-1535678 have supported the work of SYK and BAS. Thomson scattering simulations were completed utilizing high-performance computing resources of the Holland Computing Centre (HCC) of the University of Nebraska.

Author details

Serge Y. Kalmykov^{1*}, Xavier Davoine², Isaac Ghebregziabher³ and Bradley A. Shadwick¹

*Address all correspondence to: s.kalmykov.2013@ieee.org

1 Department of Physics and Astronomy, University of Nebraska–Lincoln, Lincoln, NE, USA

2 CEA DAM DIF, Arpajon, France

3 The Pennsylvania State University, Hazleton, PA, USA

References

- [1] Budker GJ. Relativistic stabilized electron beam: I. Physical principles and theory. In: Regenstreif E, editor. Proceedings of CERN Symposium on High Energy Accelerators and Pion Physics; 11-23 June 1956; Geneva, Switzerland. Geneva, Switzerland: CERN; 1956. p. 68-75. DOI: 10.5170/CERN-1956-025.68
- [2] Veksler VI. Coherent principle of acceleration of charged particles. In: Regenstreif E, editor. Proceedings of CERN Symposium on High Energy Accelerators and Pion Physics; 11-23 June 1956; Geneva, Switzerland. Geneva, Switzerland: CERN; 1956. p. 81-83. DOI: 10.5170/CERN-1956-025.80
- [3] Fainberg IaB. The use of plasma waveguides as accelerating structures in linear accelerators. In: Regenstreif E, editor. Proceedings of CERN Symposium on High Energy Accelerators and Pion Physics; 11-23 June 1956; Geneva, Switzerland. Geneva, Switzerland: CERN; 1956. p. 84-90. DOI: 10.5170/CERN-1956-025.84
- [4] Mangles SPD, Murphy CD, Najmudin Z, Thomas AGR, Collier JL, Dangor AE, et al. Monoenergetic beams of relativistic electrons from intense laser-plasma interactions. *Nature (London)*. 2004;**431**:535-538. DOI: 10.1038/nature02939
- [5] Geddes CGR, Toth Cs, van Tilborg J, Esarey E, Schroeder CB, Bruhwiler D, et al. High-quality electron beams from a laser wakefield accelerator using plasma-channel guiding. *Nature (London)*. 2004;**431**:538-541. DOI: 10.1038/nature02900
- [6] Faure J, Glinec Y, Pukhov A, Kiselev S, Gordienko S, Lefebvre E, et al. A laser-plasma accelerator producing monoenergetic electron beams. *Nature (London)*. 2004;**431**:541-544. DOI: 10.1038/nature02963
- [7] Blumenfeld I, Clayton CE, Decker F-J, Hogan MJ, Huang C, Ischebeck R, et al. Energy doubling of 42 GeV electrons in a metre-scale plasma wakefield accelerator. *Nature (London)*. 2007;**445**:741-744. DOI: 10.1038/nature05538
- [8] Corde S, Adli E, Allen JM, An W, Clarke CI, Clayton CE, et al. Multi-gigaelectronvolt acceleration of positrons in a self-loaded plasma wakefield. *Nature (London)*. 2015;**524**:442-445. DOI: 10.1038/nature14890
- [9] Tajima T, Dawson JM. Laser electron accelerator. *Physical Review Letters*. 1979;**43**(4):267-270. DOI: 10.1103/PhysRevLett.43.267
- [10] Kalmykov SY, Gorbunov LM, Mora P, Shvets G. Injection, trapping, and acceleration of electrons in a three-dimensional nonlinear laser wakefield. *Physics of Plasmas*. 2006;**13**(11):113102. DOI: 10.1063/1.2363172
- [11] Matlis NH, Reed SA, Bulanov SS, Chvykov V, Kalintchenko G, Matsuoka T, et al. Snapshots of laser wakefields. *Nature Physics*. 2006;**2**:749-753. DOI: 10.1038/nphys442
- [12] Rosenzweig JB, Breizman B, Katsouleas T, Su JJ. Acceleration and focusing of electrons in two-dimensional nonlinear plasma wake fields. *Physical Review A*. 1991;**44**(10):R6189-R6192. DOI: 10.1103/PhysRevA.44.R6189

- [13] Mora P, Antonsen TM Jr. Electron cavitation and acceleration in the wake of ultraintense, self-focused laser pulse. *Physical Review E*. 1996;**53**(3):R2068-R2071. DOI: 10.1103/PhysRevE.53.R2068
- [14] Pukhov A, Meyer-ter-Vehn J. Laser wake field acceleration: The highly non-linear broken-wave regime. *Applied Physics B: Lasers & Optics*. 2002;**74**(4–5):355-361. DOI: 10.1007/s003400200795
- [15] Kalmykov SY, Yi SA, Beck A, Lifschitz AF, Davoine X, Lefebvre E, et al. Numerical modelling of a 10-cm-long multi-GeV laser wakefield accelerator driven by a self-guided petawatt pulse. *New Journal of Physics*. 2010;**12**(4):045019. DOI: 10.1088/1367-2630/12/4/045019
- [16] Kalmykov SY, Shadwick BA, Beck A, Lefebvre E. Physics of quasi-monoenergetic laser-plasma acceleration of electrons in the blowout regime. In: Andreev AV, editor. *Femtosecond-Scale Optics*. Rijeka, Croatia: InTech; 2011. pp. 113-138. DOI: 10.5772/25062
- [17] Malka V. Laser plasma accelerators. *Physics of Plasmas*. 2012;**19**(5):055501. DOI: 10.1063/1.3695389
- [18] Lu W, Tzoufras M, Joshi C, Tsung FS, Mori WB, Vieira J, et al. Generating multi-GeV electron bunches using single stage laser wakefield acceleration in a 3D nonlinear regime. *Physical Review Accelerators and Beams*. 2007;**10**(6):061301. DOI: 10.1103/PhysRevSTAB.10.061301
- [19] Dong P, Reed SA, Yi SA, Kalmykov S, Shvets G, Downer MC, et al. Formation of optical bullets in driven plasma bubble accelerators. *Physical Review Letters*. 2010;**104**(13):134801. DOI: 10.1103/PhysRevLett.104.134801
- [20] Li Z, Tsai H-E, Zhang X, Pai C-H, Chang Y-Y, Zgadzaj R, et al. Single-shot visualization of evolving laser wakefields using an all-optical streak camera. *Physical Review Letters*. 2014;**113**(8):085001. DOI: 10.1103/PhysRevLett.113.085001
- [21] Kalmykov SY, Beck A, Yi SA, Khudik V, Shadwick BA, Lefebvre E, Downer MC. *electron* Self-injection into an evolving plasma bubble: The way to a dark current free GeV-scale laser accelerator. *AIP Conference Proceedings*. 2010;**1299**:174-179. DOI: 10.1063/1.3520309
- [22] Kalmykov SY, Beck A, Yi SA, Khudik VN, Downer MC, Lefebvre E, et al. Electron self-injection into an evolving plasma bubble: Quasi-monoenergetic laser-plasma acceleration in the blowout regime. *Physics of Plasmas*. 2011;**18**(5):056704. DOI: 10.1063/1.3566062
- [23] Kalmykov SY, Beck A, Davoine X, Lefebvre E, Shadwick BA. Laser plasma acceleration with a negatively chirped pulse: All-optical control over dark current in the blowout regime. *New Journal of Physics*. 2012;**14**(3):033025. DOI: 10.1088/1367-2630/14/3/033025
- [24] Kalmykov SY, Davoine X, Lehe R, Lifschitz AF, Shadwick BA. Optical control of electron phase space in plasma accelerators with incoherently stacked laser pulses. *Physics of Plasmas*. 2015;**22**(5):056701. DOI: 10.1063/1.4920962

- [25] Kalmykov SY, Davoine X, Ghebregziabher I, Lehe R, Lifschitz AF, Shadwick BA. Controlled generation of comb-like electron beams in plasma channels for polychromatic Thomson γ -ray sources. *Plasma Physics and Controlled Fusion*. 2016;**58**(3):034006. DOI: 10.1088/0741-3335/58/3/034006
- [26] Tzoufras M, Lu W, Tsung FS, Huang C, Mori WB, Katsouleas T, et al. Beam loading by electrons in nonlinear plasma wakes. *Physics of Plasmas*. 2009;**16**(5):056705. DOI: 10.1063/1.3118628
- [27] Sun G-Z, Ott E, Lee YC, Guzdar P. Self-focusing of short intense pulses in plasmas. *The Physics of Fluids*. 1987;**30**(2):526-532. DOI: 10.1063/1.866349
- [28] Mora P, Antonsen Jr TM. Kinetic modeling of intense, short laser pulses propagating in tenuous plasmas. *Physics of Plasmas*. 1997;**4**(1):217-229. DOI: 10.1063/1.872134
- [29] Thomas AGR, Najmudin Z, Mangles SPD, Murphy CD, Dangor AE, Kamperidis C, et al. The effect of laser focusing conditions on propagation and monoenergetic electron production in laser wakefield accelerators. *Physical Review Letters*. 2007;**98**(9):095004. DOI: 10.1103/PhysRevLett.98.095004
- [30] Thomas AGR, Mangles SPD, Murphy CD, Dangor AE, Foster PS, Gallacher JG, et al. Ultrashort pulse filamentation and monoenergetic electron beam production in LWFA's. *Plasma Physics and Controlled Fusion*. 2009;**51**(2):024010. DOI: 10.1088/0741-3335/51/2/024010
- [31] Pai C-H, Chang Y-Y, Ha L-C, Xie Z-H, Lin M-W, Lin J-M, et al. Generation of intense ultrashort midinfrared pulses by laser-plasma interaction in the bubble regime. *Physical Review A*. 2010;**82**(6):063804. DOI: 10.1103/PhysRevA.82.063804
- [32] Zhu W, Palastro JP, Antonsen Jr TM. Pulsed mid-infrared radiation from spectral broadening in laser wakefield simulations. *Physics of Plasmas*. 2013;**20**(7):073103. DOI: 10.1063/1.4813245
- [33] Gordon DF, Hafizi B, Hubbard RF, Peano JR, Sprangle P, Ting A. Asymmetric self-phase modulation and compression of short laser pulses. *Physical Review Letters*. 2003;**90**(21):215001. DOI: 10.1103/PhysRevLett.90.215001
- [34] Beck A, Kalmykov SY, Davoine X, Lifschitz A, Shadwick BA, Malka V, Specka A. Physical processes at work in sub-30fs, PW laser pulse-driven plasma accelerators: Towards GeV electron acceleration experiments at CILEX facility. *Nuclear Instruments and Methods in Physics Research Section A: Accelerators, Spectrometers, Detectors and Associated Equipment*. 2014;**740**:67-73. DOI: 10.1016/j.nima.2013.11.003
- [35] Banerjee S, Powers ND, Ramanathan V, Ghebregziabher I, Brown KJ, Maharjan CM, et al. Generation of tunable, 100–800 MeV quasi-monoenergetic electron beams from a laser-wakefield accelerator in the blowout regime. *Physics of Plasmas*. 2012;**19**(5):056703. DOI: 10.1063/1.4718711

- [36] Bayramian AJ, Armstrong JP, Beer G, Campbell R, Cross R, Erlandson A, et al. High average power petawatt laser pumped by the mercury laser for fusion materials engineering. *Fusion Science and Technology*. 2009;**56**:295-300
- [37] Fattahi H, Barros HG, Gorjan M, Nubbemeyer T, Alsaif B, Teyssset CY, et al. Third-generation femtosecond technology. *Optica*. 2014;**1**(1):45-63. DOI: 10.1364/OPTICA.1.000045
- [38] Cowan BM, Kalmykov SY, Beck A, Davoine X, Bunkers K, Lifschitz AF, et al. Computationally efficient methods for modelling laser wakefield acceleration in the blowout regime. *Journal of Plasma Physics*. 2012;**78**(4):469-482. DOI: 10.1017/S0022377812000517
- [39] Kneip S, Nagel SR, Martins SF, Mangles SPD, Bellei C, Chekhlov O, et al. Near-GeV acceleration of electrons by a nonlinear plasma wave driven by a self-guided laser pulse. *Physical Review Letters*. 2009;**103**(3):035002. DOI: 10.1103/PhysRevLett.103.035002
- [40] Kneip S, Nagel SR, Bellei C, Chekhlov O, Clarke RJ, Delerue N, et al. Study of near-GeV acceleration of electrons in a non-linear plasma wave driven by a self-guided laser pulse. *Plasma Physics and Controlled Fusion*. 2011;**53**(1):014008. DOI: 10.1088/0741-3335/53/1/014008
- [41] Froula DH, Clayton CE, Döppner T, Marsh KA, Barty CPJ, Divol L, et al. Measurements of the critical power for self-injection of electrons in a laser wakefield accelerator. *Physical Review Letters*. 2009;**103**(21):215006. DOI: 10.1103/PhysRevLett.103.215006
- [42] Ralph JE, Clayton CE, Albert F, Pollock BB, Martins SF, Pak AE, et al. Laser wakefield acceleration at reduced density in the self-guided regime. *Physics of Plasmas*. 2010;**17**(5):056709. DOI: 10.1063/1.3323083
- [43] Corde S, Ta Phuoc K, Lambert G, Fitour R, Malka V, Rousse A. Femtosecond x rays from laser-plasma accelerators. *Reviews of Modern Physics*. 2013;**85**(1):1-48. DOI: 10.1103/RevModPhys.85.1
- [44] Lau YY, Fei He F, Umstadter DP, Kowalczyk R. Nonlinear Thomson scattering: A tutorial. *Physics of Plasmas*. 2003;**10**(3):2155-2162. DOI: 10.1063/1.1565115
- [45] Sarachik ES, Schappert GT. Classical theory of the scattering of intense laser radiation by free electrons. *Physical Review D*. 1970;**1**(10):2738-2753. DOI: 10.1103/PhysRevD.1.2738
- [46] Esarey E, Ride SK, Sprangle P. Nonlinear Thomson scattering of intense laser pulses from beams and plasmas. *Physical Review E*. 1993;**48**(4):3003-3021. DOI: 10.1103/PhysRevE.48.3003
- [47] Ride SK, Esarey E, Baine M. Thomson scattering of intense lasers from electron beams at arbitrary interaction angles. *Physical Review E*. 1995;**52**(5):5425-5442. DOI: 10.1103/PhysRevE.52.5425
- [48] Albert F, Anderson SG, Gibson DJ, Marsh RA, Wu SS, Siders CW, et al. Design of narrow-band Compton scattering sources for nuclear resonance fluorescence. *Physical Review Accelerators and Beams*. 2011;**14**(5):050703. DOI: 10.1103/PhysRevSTAB.14.050703

- [49] Rykovanov SG, Geddes CGR, Vay J-L, Schroeder CB, Esarey E, Leemans WP. Quasi-monoenergetic femtosecond photon sources from Thomson scattering using laser plasma accelerators and plasma channels. *Journal of Applied Physics B: Atomic, Molecular and Optical Physics*. 2014;**47**(23):234013. DOI: 10.1088/0953-4075/47/23/234013
- [50] Tomassini P, Giulietti A, Giulietti D, Gizzi LA. Thomson backscattering X-rays from ultra-relativistic electron bunches and temporally shaped laser pulses. *Applied Physics B: Lasers & Optics*. 2005;**80**(4–5):419-436. DOI: 10.1007/s00340-005-1757-x
- [51] Ghebregziabher I, Shadwick BA, Umstadter DP. Spectral bandwidth reduction of Thomson scattered light by pulse chirping. *Physical Review Accelerators and Beams*. 2013; **16**(3):030705. DOI: 10.1103/PhysRevSTAB.16.030705
- [52] Kalmykov SY, Davoine X, Ghebregziabher I, Shadwick BA. Multi-color γ -rays from comb-like electron beams driven by incoherent stacks of laser pulses. *AIP Conference Proceedings*. 2017;**1812**:100001. DOI: 10.1063/1.4975899
- [53] Hsu IC, Chu C-C, Yu C-I. Energy measurement of relativistic electron beams by laser Compton scattering. *Physical Review E*. 1996;**54**(5):5657-5663. DOI: 10.1103/PhysRevE.54.5657
- [54] Baylac M, Burtin E, Cavata C, Escoffier S, Frois B, Lhuillier D, et al. First electron beam polarization measurements with a Compton polarimeter at Jefferson Laboratory. *Physics Letters B*. 2002;**539**:8-12. DOI: 10.1016/S0370-2693(02)02091-9
- [55] Omori T, Fukuda M, Hirose T, Kurihara Y, Kuroda R, Nomura M, et al. Efficient propagation of polarization from laser photons to positrons through Compton scattering and electron-positron pair creation. *Physical Review Letters*. 2006;**96**(11):114801. DOI: 10.1103/PhysRevLett.96.114801
- [56] Kikuzawa N, Hajima R, Nishimori N, Minehara E, Hayakawa T, Shizuma T, et al. Non-destructive detection of heavily shielded materials by using nuclear resonance fluorescence with a laser-Compton scattering γ -ray source. *Applied Physics Express*. 2009;**2**:036502. DOI: 10.1143/APEX.2.036502
- [57] Hajima R, Kikuzawa N, Nishimori N, Hayakawa T, Shizuma T, Kawase K, et al. Detection of radioactive isotopes by using laser Compton scattered gamma-ray beams. *Nuclear Instruments and Methods in Physics Research Section A: Accelerators, Spectrometers, Detectors and Associated Equipment*. 2009;**608**:S57-S61. DOI: 10.1016/j.nima.2009.05.063
- [58] Hayakawa T, Ohgaki H, Shizuma T, Hajima R, Kikuzawa N, Minehara E, et al. Non-destructive detection of hidden chemical compounds with laser Compton-scattering gamma rays. *Review of Scientific Instruments*. 2009;**80**(4):045110. DOI: 10.1063/1.3125022
- [59] Albert F, Anderson SG, Anderson GA, Betts SM, Gibson DJ, Hagmann CA, et al. Isotope-specific detection of low-density materials with laser-based monoenergetic gamma-rays. *Optics Letters*. 2010;**35**(3):354-356. DOI: 10.1364/OL.35.000354

- [60] Albert F, Anderson SG, Gibson DJ, Hagmann CA, Johnson MS, Messerly M, et al. Characterization and applications of a tunable, laser-based MeV-class Compton-scattering γ -ray source. *Physical Review Accelerators and Beams*. 2010;**13**(7):070704. DOI: 10.1103/PhysRevSTAB.13.070704
- [61] Ohgaki H, Daito I, Zen H, Kii T, Masuda K, Misawa T, et al. Nondestructive inspection system for special nuclear material using inertial electroelastic confinement fusion neutrons and laser Compton scattering gamma-rays. *IEEE Transactions on Nuclear Science*. 2017;**64**(7):1635-1640. DOI: 10.1109/TNS.2017.2652619
- [62] Jochmann A, Irman A, Bussmann M, Couperus JP, Cowan TE, Debus AD, et al. High resolution energy-angle correlation measurement of hard X rays from laser-Thomson backscattering. *Physical Review Letters*. 2013;**111**(11):114803. DOI: 10.1103/PhysRevLett.111.114803
- [63] Ta Phuoc K, Rousse A, Pittman M, Rousseau JP, Malka V, Fritzler S, et al. X-ray radiation from nonlinear Thomson scattering of an intense femtosecond laser on relativistic electrons in helium plasma. *Physical Review Letters*. 2003;**91**(19):195001. DOI: 10.1103/PhysRevLett.91.195001
- [64] Schwoerer H, Liesfeld B, Schlenvoigt H-P, Amthor K-U, Sauerbrey R, Thomson-backscattered X. Rays from laser-accelerated electrons. *Physical Review Letters*. 2006;**96**(1):014802. DOI: 10.1103/PhysRevLett.96.014802
- [65] Ta Phuoc K, Corde S, Thaury C, Malka V, Tafzi A, Goddet JP, et al. All-optical Compton gamma-ray source. *Nature Photonics*. 2012;**6**(5):308-311. DOI: 10.1038/NPHOTON.2012.82
- [66] Chen S, Powers ND, Ghebregziabher I, Maharjan CM, Liu C, Golovin G, et al. MeV-energy X rays from inverse Compton scattering with laser-wakefield accelerated electrons. *Physical Review Letters*. 2013;**110**(15):155003. DOI: 10.1103/PhysRevLett.110.155003
- [67] Powers ND, Ghebregziabher I, Golovin G, Liu C, Chen S, Banerjee S, et al. Quasi-monoenergetic and tunable X-rays from a laser-driven Compton light source. *Nature Photonics*. 2014;**8**:28-31. DOI: 10.1038/nphoton.2013.314
- [68] Sarri G, Corvan DJ, Schumaker W, Cole JM, Di Piazza A, Ahmed H, et al. Ultrahigh brilliance multi-MeV γ -ray beams from nonlinear relativistic Thomson scattering. *Physical Review Letters*. 2014;**113**(22):224801. DOI: 10.1103/PhysRevLett.113.224801
- [69] Miura E, Ishii S, Tanaka K, Kuroda R, Toyokawa H. X-ray pulse generation by laser Compton scattering using a high-charge, laser-accelerated, quasi-monoenergetic electron beam. *Applied Physics Express*. 2014;**7**:046701. DOI: 10.7567/APEX.7.046701
- [70] Tsai H-E, Wang X, Shaw JM, Li Z, Arefiev AV, Zhang X, et al. Compact tunable Compton x-ray source from laser-plasma accelerator and plasma mirror. *Physics of Plasmas*. 2015;**22**(2):023106. DOI: 10.1063/1.4907655

- [71] Khrennikov K, Wenz J, Buck A, Xu J, Heigoldt M, Veisz L, Karsch S. Tunable all-optical quasimonochromatic Thomson X-ray source in the nonlinear regime. *Physical Review Letters*. 2015;**114**(19):195003. DOI: 10.1103/PhysRevLett.114.195003
- [72] Liu C, Golovin G, Chen S, Zhang J, Zhao B, Haden D, et al. Generation of 9 MeV γ -rays by all-laser-driven Compton scattering with second-harmonic laser light. *Optics Letters*. 2014;**39**(14):4132-4135. DOI: 10.1364/OL.39.004132
- [73] Shaw JM, Bernstein AC, Hannasch A, LaBerge M, Chang Y-Y, Weichman K, et al. Generation of tens-of-MeV photons by Compton backscatter from laser-plasma-accelerated GeV electrons. *AIP Conference Proceedings*. 2017;**1812**:100012. DOI: 10.1063/1.4975910
- [74] Scoby CM. Adapting High Brightness Relativistic Electron Beams for Ultrafast Science [Dissertation]. Los Angeles, California, USA: The University of California; 2013. 165 p. Available from: <http://escholarship.org/uc/item/11p8s2h1>
- [75] Lundh O, Lim J, Rechatin C, Ammoura L, Ben-Ismaïl A, Davoine X, et al. Few-femtosecond, few kiloampere electron bunch produced by a laser-plasma accelerator. *Nature Physics*. 2011;**7**:219-222. DOI: 10.1038/nphys1872
- [76] Cianchi A, Anania MP, Bisesto F, Castellano M, Chiadroni E, Pompili R. Observations and diagnostics in high brightness beams. *Nuclear Instruments and Methods in Physics Research Section A: Accelerators, Spectrometers, Detectors and Associated Equipment*. 2016;**829**:343-347. DOI: 10.1016/j.nima.2016.03.076
- [77] Gizzi LA, Benedetti C, Cecchetti CA, Di Pirro G, Gamucci A, Gatti G, et al. Laser-plasma acceleration with *FLAME* and *ILIL* ultraintense lasers. *Applied Sciences*. 2013;**3**:559-580. DOI: 10.3390/app3030559
- [78] Zou JP, Le Blanc C, Papadopoulos DN, Chériaux G, Georges P, Mennerat G, et al. Design and current progress of the Apollon 10 PW project. *High Power Laser Science and Engineering*. 2015;**3**:e2. DOI: 10.1017/hpl.2014.41
- [79] Agrawal GP. *Nonlinear Fiber Optics*. 4th ed. San Diego: Academic Press; 2006. 529 p. DOI: 10.1016/B978-012369516-1/50000-5
- [80] Benedetti C, Schroeder CB, Esarey E, Leemans WP. Plasma wakefields driven by an incoherent combination of laser pulses: A path towards high-average power laser-plasma accelerators. *Physics of Plasmas*. 2014;**21**(5):056706. DOI: 10.1063/1.4878620
- [81] Vargas M, Schumaker W, He Z-H, Behm K, Chvykov V, Hou B, et al. Improvements to laser wakefield accelerated electron beam stability, divergence, and energy spread using three-dimensional printed two-stage gas cell targets. *Applied Physics Letters*. 2014;**104**(17):174103. DOI: 10.1063/1.4874981
- [82] He Z-H, Hou B, Nees JA, Easter JH, Faure J, Krushelnick K, Thomas AGR. High repetition-rate wakefield electron source generated by few-millijoule, 30 fs laser pulses on a density downramp. *New Journal of Physics*. 2013;**15**(5):053016. DOI: 10.1088/1367-2630/15/5/053016

- [83] He Z-H, Hou B, Lebailly V, Nees1 JA, Krushelnick K, Thomas AGR. Coherent control of plasma dynamics. *Nature Communications*. 2015;**6**:7156. DOI: 10.1038/ncomms8156
- [84] Zhu W, Palastro JP, Antonsen Jr TM. Studies of spectral modification and limitations of the modified paraxial equation in laser wakefield simulations. *Physics of Plasmas*. 2012;**19**(3):033105. DOI: 10.1063/1.3691837
- [85] Lifschitz AF, Davoine X, Lefebvre E, Faure J, Rechatin C, Malka V. Particle-in-cell modeling of laser-plasma interaction using Fourier decomposition. *Journal of Computational Physics*. 2009;**228**:1803-1814. DOI: 10.1016/j.jcp.2008.11.017
- [86] Lehe R, Lifschitz A, Thaury C, Malka V, Davoine X. Numerical growth of emittance in simulations of laser-wakefield acceleration. *Physical Review Accelerators and Beams*. 2013;**16**(2):021301. DOI: 10.1103/PhysRevSTAB.16.021301
- [87] Jackson JD. *Classical Electrodynamics*. 3rd ed. New York: Wiley; 1999. 832 p
- [88] Balakin AA, Litvak AG, Mironov VA, Skobelev SA. Compression of femtosecond petawatt laser pulses in a plasma under the conditions of wake-wave excitation. *Physical Review A*. 2013;**88**(2):023836. DOI: 10.1103/PhysRevA.88.023836
- [89] Schreiber J, Bellei C, Mangles SPD, Kamperidis C, Kneip S, Nagel SR, et al. Complete temporal characterization of asymmetric pulse compression in a laser wakefield. *Physical Review Letters*. 2010;**105**(23):235003. DOI: 10.1103/PhysRevLett.105.235003
- [90] Weingartner R, Fuchs M, Popp A, Raith S, Becker S, Chou S, et al. Imaging laser-wakefield-accelerated electrons using miniature magnetic quadrupole lenses. *Physical Review Accelerators and Beams*. 2011;**14**(5):052801. DOI: 10.1103/PhysRevSTAB.14.052801
- [91] Grigsby FB, Dong P, Downer MC. Chirped-pulse Raman amplification for two-color, high-intensity laser experiments. *Journal of the Optical Society of America B*. 2008;**25**(3):346-350. DOI: 10.1364/JOSAB.25.000346
- [92] Sanders JC, Zgadzaj R, Downer MC. Two-color terawatt laser system for high-intensity laser-plasma experiments. *AIP Conference Proceedings*. 2012;**1507**:882-886. DOI: 10.1063/1.4773816
- [93] Vicario C, Shalaby M, Konyashchenko A, Losev L, Hauri CP. High-power femtosecond Raman frequency shifter. *Optics Letters*. 2016;**41**(20):4719-4722. DOI: 10.1364/OL.41.004179

